Identifying Tethys oceanic fingerprint in post-collisional potassium-rich lavas in Tibet using thallium isotopes

Feixiang Wei[a,b,c], Julie Prytulak[c,d], Evelyn B. Baker[c]., Jiandong Xu[a,b], Bo Zhao[a,b]

[a] Jilin Changbaishan Volcano National Observation and Research Station, Institute of Geology, China Earthquake Administration (CEA), Beijing 100029, China

[b] Key Laboratory of Seismic and Volcanic Hazards, CEA, Beijing 100029, China

[c] Department of Earth Science and Engineering, Imperial College London, SW7 2AZ, UK

[d] Department of Earth Sciences, University of Durham, DH1 3LE, UK

Highlights

Thallium concentrations in lavas higher than partial melts of a primitive mantle.

Thallium isotopes distinguish between continental and oceanic components.

Evidence for minor kinetic isotope fractionation via degassing.

Phlogopite is an important host mineral for Tl.

Keywords:

Tibetan magmatism

Potassium-rich lavas

Thallium isotope

Degassing

Tethys Ocean

Abstract

Following the Indian-Asian continental collision, the Tibetan Plateau experienced continuous magmatism from south to north, most of which is characterized by high potassium (K) content and negative niobium-tantalum-titanium (Nb-Ta-Ti) anomalies. We performed the first exploration using thallium (Tl) isotopes as potential tracers of the source of post-collisional K-rich magmatism. A case study on Tl isotope systematics of K-rich lavas in Ashikule volcanic basin (AVB) in northwestern Tibet is provided, which represents the youngest volcanism in Tibet. Thallium abundances of the AVB

lavas are significantly enriched compared to other magmatic settings, with concentrations from 148 to 8259 ng/g. Thallium isotope ratios (reported as $\varepsilon^{205}Tl$) extend to some of the heaviest yet measured in igneous materials, with a range of $\varepsilon^{205}Tl$ between -2.7 and +6.4 ε-units. We evaluate if secondary processes can account for the range in Tl isotope ratios, systematically examining the influences of alteration, degassing, fractional crystallization, and assimilation. Only two samples appear to be influenced by secondary processes, interpreted as kinetic fractionation during degassing, and one sample may be contaminated by sulfides with coupled elevated Tl and Pb contents. The remainder of the Tl isotope ratio range (-2.0 to +5.1 ε-units) we interpret to reflect the source region(s) from which the magmas are derived. The AVB lavas have restricted strontium and neodymium isotopes, suggestive of a homogeneous source, and therefore an apparent decoupling of radiogenic and stable isotope systems is apparent in these lavas. The variation in Tl isotope ratios is interpreted to reflect the contribution of oceanic sediments, which may be associated with ancient Paleo- and Neo-Tethys subductions.

1. Introduction

Cenozoic K-rich lavas are widely distributed on the Tibetan Plateau (Fig. 1) due to the northward subduction of the Indian plate beneath the Tibetan Plateau since ~55 Ma (e.g., Tapponnier et al., 2001; Ding et al., 2003). These post-collisional lavas are generally characterized by negative Nb-Ta-Ti anomalies and enriched strontium-neodymium-lead (Sr-Nd-Pb) isotopes, indicating an enriched mantle source (Williams et al., 2004; Chung et al., 2005; Wei et al., 2017; Wang et al., 2020a). However, there is much debate about where those enriched components were inherited, especially in northwestern Tibet with the addition of the south-subducting Asian plate (e.g., Turner et al., 1993, 1996; Williams et al., 2004; Guo et al., 2014; Wei et al., 2017; Guo and Wilson, 2019; Yuan et al., 2020; Wang et al., 2020a).

Several geodynamic models have been proposed to explain the origin of the enriched components in post-collisional lavas in northwestern Tibet. Considering that the Tibetan Plateau underwent long-term Tethys Ocean subductions before the Indian-

Asian collision, some studies attribute the enriched components to Tethyan materials trapped in the metasomatized lithospheric mantle (e.g., Turner et al., 1996; Williams et al., 2004; Wei et al., 2017; Wang et al., 2020a; Yuan et al., 2020). The volcanoes in the northwestern Tibetan Plateau are spatially close to the Tarim block (Asian plate) (Fig. 1), and thus the material contributions of the Tarim block should be considered. Additionally, magmatic rocks in northwestern Tibet exhibit similar Sr-Pb isotopes to the Asian plate endmember, suggesting a dominant Asian plate source for those rocks (Guo and Wilson, 2019). The Asian plate is continental, whereas the ancient Tethys plates are oceanic (Wu et al., 2020). Therefore, recent magmatism in northwestern Tibet provides an ideal laboratory to identify the enriched components in the lavas if we can distinguish continental and oceanic fingerprints in the lavas.

In recent years, Tl isotopic compositions have been increasingly applied to track recycling of oceanic sediments and slab-derived fluids in igneous rocks from subduction and plume settings (e.g., Nielsen et al., 2006a, 2007, 2016, 2017a; Prytulak et al., 2013; Shu et al., 2017, 2019, 2022; Blusztajn et al., 2018; Brett et al., 2021; Williamson et al. 2021). Thallium has two stable isotopes, ^{203}Tl and ^{205}Tl, and isotopic variations are reported in epsilon notation relative to NIST Tl standard SRM997, which is defined as zero, by the equation:

$$\varepsilon^{205}Tl = 10{,}000 \times [(^{205}Tl/^{203}Tl_{sample} - ^{205}Tl/^{203}Tl_{SRM997})/(^{205}Tl/^{203}Tl_{SRM997})]$$

Thallium is a heavy metal with a large ionic radius (Tl^{+}=1.49Å; Shaw, 1952), whose oxidation states are Tl^{+} and Tl^{3+}. Due to the similar ionic characteristics between Tl^{+} and alkali metals, Tl preferentially replaces K, rubidium (Rb), and cesium (Cs) elements and forms isomorphous structures in minerals (Wedepohl, 1974; Hernrichs et al., 1980). Theoretical calculations show that chemical reactions with both valence states (Tl^{+} and Tl^{3+}) can cause significant equilibrium Tl isotopic fractionation (Schauble, 2007). However, Tl^{3+} is not stable under seawater conditions (Nielsen et al., 2009), and Tl exhibits strong correlations with alkali metals in continental crust, indicating Tl^{+} is the dominant valence state in minerals. Apart from ionic bonds, Tl tends to form covalent bonds and be enriched in sulfides (Nielsen et al., 2014; Genna and Gaboury, 2015). Highly incompatible properties of Tl during partial melting and

fractional crystallization (Shaw, 1952) result in significantly high Tl concentrations in the continental crust (~0.5 μg/g; Heinrichs et al., 1980) compared to the primitive mantle (0.0035 μg/g; McDonough and Sun, 1995).

There are several key advantages to using Tl isotopes to distinguish oceanic versus continental inputs to igneous rocks: 1) Tl isotopes do not appear to fractionate during partial melting, and the upper mantle appears to have a relatively homogeneous Tl isotopic composition of around ε^{205}Tl= -2±1 (e.g., Nielsen et al. 2005, 2006a, 2007) 2) Tl isotopes do not fractionate during magmatic evolution and fractionation of anhydrous minerals (e.g., Prytulak et al., 2017; Nielsen et al., 2017b; Gaschnig et al., 2021) and 3) Tl isotopes do not appear to fractionate during fluid release from subducting slabs (Shu et al. 2022). Against the backdrop of insensitivity to partial melting, fractional crystallization, and fluid release, Tl isotopes can be significantly fractionated by low-temperature processes, alteration, and degassing (e.g., Baker et al., 2009; Nielsen et al., 2005). For example, low-temperature altered oceanic crust, pelagic clays, and ferromanganese (Fe-Mn) sediments are characterized by enriched Tl concentrations and variable Tl isotopes.

In the oceanic realm, large Tl isotopic variations are observed, with ε^{205}Tl varying from around -16 of low-temperature altered ocean crust (Nielsen et al., 2006b) to around +15 of marine Fe-Mn sediments (Rehkämper et al., 2002; Peacock and Moon, 2012). In contrast, continent-derived sediments have orders of magnitude lower Tl concentrations and more restricted isotopic values around ε^{205}Tl = -2, similar to the upper mantle (e.g., Nielsen et al., 2016, 2017b; Shu et al., 2022). Therefore, the addition of continental sediments to a mantle source is less likely to modify the Tl isotopic composition of igneous rocks than the addition of oceanic sediments.

The above characteristics make Tl a useful tool to distinguish oceanic versus continental components in the source of post-collisional lavas in northeastern Tibet, and thus evaluate competing theories of their formation. Our previous work on the AVB lavas on Tibet Plateau revealed high Tl concentrations up to 8.3 μg/g (Wei et al., 2017). Moreover, Tl-rich minerals (e.g., phlogopite) have been detected in several samples and the AVB lavas are suggested to be derived from a phlogopite-bearing peridotite source

(Wei et al., 2017). In this study, we undertook a Tl isotope study of post-collisional lavas from AVB in northwestern Tibet, to try and identify the enriched components in post-collisional lavas in Tibet, and explore the application of Tl isotope in K-rich volcanic rocks.

2. Geological settings

In response to the gradual subduction of the Indian plate beneath the Tibetan Plateau from ~55 Ma ago, a series of complex tectonic events and magmatism took place progressively from south to north Tibet (Fig. 1) (e.g., Tapponnier et al., 2001; Ding et al., 2003). Post-collisional lavas are commonly enriched in K and incompatible elements, and exhibit negative Nb-Ta-Ti anomalies (Turner et al., 1996; Williams et al., 2004). According to their spatial and temporal distributions, they can be divided into four principal east-west magma suites (Fig. 1; Ding et al., 2003; Chung, et al., 2005), which may be attributed to the northward subduction of the Indian plate and the resisting Tarim and Qaidam lithospheres (Chung et al., 2005).

The northernmost magma suite mainly in Songpan-Ganzi terrane is the youngest, with eruptions from 17 Ma to the present (Ding et al., 2003; Chung et al., 2005). Lavas in this suite are commonly shoshonites, whereas the lavas from the other suites retain a wider range of K_2O contents, from shoshonitic to ultrapotassic series (Williams et al., 2004; Chung et al., 2005). Located in the west part of the Songpan-Ganzi magma suite, the AVB covers an area of ~700 km^2, and 14 volcanoes have been recognized with eruptions from 2.80 Ma to 1951 AD (Liu and Maimaiti, 1989; Xu et al., 2014). The 1951 AD eruption of the Ashi Volcano in the AVB is regarded as the most recent eruption in Tibet (Liu and Maimaiti, 1989). The AVB is a pull-part basin, structurally controlled by Altyn Tagh, Karakax, and Longmu-Gozha Co fault systems. Seismic tomography suggests that the upper mantle beneath this area is compressed by the Indian plate in the south and Tarim block in the north, with a small gap between them (Wei et al., 2017). As a result, the AVB and adjacent area are seismically active, with at least 20 Mw $\geq$ 5 earthquakes since 2000 (Global Centroid-Moment-Tensor catalogue, www.globalcmt.org).

3. Prior work and samples

Prior geochemical work (Wei et al., 2017) shows that the AVB lavas are mainly basaltic trachyandesite with relatively high K_2O contents between 3.48 and 4.47 wt%. These post-collisional lavas are characterized by negative Nb-Ta-Ti anomalies, remarkably enriched light rare earth elements (LREE) relative to heavy rare earth elements (HREE), and enriched Sr-Nd isotopes ($^{87}Sr/^{86}Sr$ = 0.707490–0.710523; $^{143}Nd/^{144}Nd$ = 0.512265–0.512472) relative to bulk silicate earth, suggesting a subduction-related source (Wei et al., 2017). Combining with the geochemical and geophysical perspectives, partial melting of a previously metasomatized phlogopite-bearing peridotite source in the subcontinental lithospheric mantle (SCLM) was suggested (Wei et al., 2017).

From the 25 samples measured by Wei et al. (2017), 20 samples with Sr-Nd isotopic data were selected for Tl isotope analysis. All the studied lava samples are porphyritic in texture, with vesicles ranging from 10% to 80% in volume. The petrography of the samples has been discussed in Wei et al. (2017), but we reiterate key features in Table 1. To clarify the abnormally high concentration of Tl in sample ASKL-3 (8.3 μg/g), the volume and composition of sulfides in the thin section were studied using scanning electron microscopy (SEM) and electron probe microanalysis (EPMA).

4. Methods

4.1 Thallium isotopic analysis

All sample processing and measurements took place in the MAGIC laboratories at Imperial College London. All acids used were quartz distilled (HNO_3, HCl) or ultrapure Romil (HF, Br_2).

4.1.1 Leaching and digestion

Thallium readily substitutes for K in crystallographic sites, therefore, secondary K-rich alteration materials such as clays can contain significant Tl. To assess any potential effect of surficial alteration on Tl isotope ratios, we compared the isotopic compositions

of leached and unleached samples. We pre-leached samples according to the procedure of Weis and Frey (1991, 1996). Briefly, approximately 150 mg rock powder was leached with 6M HCl (Weis and Frey, 1991, 1996) to eliminate the influence of secondary minerals. Approximately 50 mg of powder was digested for unleached samples. Both leached and unleached samples were digested using standard techniques employing initial digestion with 1 ml concentrated HNO_3 and 3 ml concentrated HF on a hotplate set at 160 ℃ for two days. Then they were evaporated at 180℃ to near dryness. Around 0.5 ml concentrated HNO_3 was added to the samples and evaporated to remove SiF_4 in the solutions. This SiF_4-remove step was repeated 3-5 times until the solid samples turned brown or brownish. Around 1 ml 6M HCl was added and evaporated twice. Subsequently, the samples were digested in 2ml 6M HCl for 24 hours at 120℃. The samples were visually inspected for complete dissolution before chemical separation.

4.1.2 Chemical separation of Tl

Chemical separation of Tl was conducted by a two-stage column chemistry following the methods of Rehkämper and Halliday (1999) and Nielsen et al. (2004) and modified by Brett et al. (2018). Briefly, Tl was oxidized to Tl^{3+} by water-saturated Br_2 and formed anionic complexes with Cl^-. When eluting the major and trace elements with HNO_3-Br_2 mixed solutions, Tl anionic complexes were retained on the anion exchange resin. Afterwards, Tl was collected by adding water-saturated SO_2 to reduce Tl^{3+} to Tl^+, which can be easily eluted from the resin. This whole separation step was repeated using smaller Teflon columns to further purify the Tl solutions from the rest of the matrix and to reduce the residual sulfuric acid before the mass spectrometry.

4.1.3 MC-ICPMS measurement

Thallium isotopic compositions were collected using a Nu Instruments HR Multi-collector Inductively Coupled Plasma Mass Spectrometer (MC-ICPMS) and on a Nu Plasma II machine with the same setup in the MAGIC laboratories at Imperial College London. Following the method of Rehkämper and Halliday (1999), all solutions were

diluted to between 1 and 5 ng/g, depending on machine sensitivity, and were doped to Pb/Tl ratios of ~4 using NIST SRM981 Pb for external correction for mass discrimination. NIST SRM997 Tl was used for sample-standard bracketing to calculate the ε^{205}Tl of measured samples.

Long-term measurements of the secondary solution standard "Aldrich" against NIST SRM997 Tl in the MAGIC laboratories is -0.8±0.3 (2sd, n=211) which is in excellent agreement with literature values (see overview in Nielsen et al. 2017b and Brett et al. 2018). USGS reference material BCR-2 was also measured for quality control and repeat measurements of the same solution of BCR-2 display ε^{205}Tl = -2.02±0.55 (2sd, n=4), which is close to -2.5±0.4 as compiled in Nielsen et al. (2017b).

4.2 SEM and EPMA measurements of sample ASKL-3

The thin section of ASKL-3 was coated with carbon for SEM and EPMA measurements at the Wuhan Sample Solution Analytical Technology Co. Ltd. (China). A JEOL JSM-IT300 (JEOL, Japan) analytical scanning electron microscope was used for imaging under the accelerating voltage of 15 kV. A JEOL JXA-8230 (JEOL, Japan) electron probe micro-analyzer was used to measure the major and minor concentrations under the following operation conditions: 20 kV accelerating voltage, 20 nA beam current, and 0.5 μm spot size. The calibration standards for Pb (galena), Tl (thallium bromide iodide), Fe (pyrite), S (pyrite), As (arsenopyrite), Se (bismuth selenide), Zn (zinc sulfide), Ni (pentlandite), and Cu (copper iron sulfide) were used.

5. Results

5.1 Thallium isotope geochemistry

The leaching results for Tl isotopes are shown in Fig. 2. Except for sample ASKL-14, all the leached AVB lavas display Tl isotopic compositions within error of unleached values, which reinforces the fresh petrologic nature of the AVB lavas. Sample ASKL-14 exhibits Tl isotopes (ε^{205}Tl) of +1.8 ε-units (unleached) versus -0.3 ε-units (leached), and thus leached value of this sample is used in the subsequent

discussion.

Chemical and isotopic compositions of Tl of the AVB lavas are presented in Table 2. Thallium concentrations of the AVB lavas are significantly higher than those of arc lavas, mid-ocean ridge basalt (MORB), and ocean island basalt (OIB) (Fig. 3), ranging from 0.148 to 8.3 μg/g, with an average value of 1.13 μg/g. Sample ASKL-3 displays an extremely high Tl concentration of 8.3 μg/g. To confirm this abnormally high Tl concentration, we re-measured the Tl concentration following the methods in Wei et al. (2017) and acquired a close value of 7.1 μg/g. Sample ASKL-3 is also distinguished from other samples by its highest content of vesicles. However, Tl concentrations of the AVB lavas do not correlate with their vesicle contents (not shown). The remainder of the samples exhibits Tl concentrations between 0.148 to 1.96 μg/g. The cerium/thallium ratios (Ce/Tl) of the AVB lavas are highly variable, ranging from 37 to 2022 (Table 2; Fig. 4). Sample 513-11 and ASKL-7 display significantly high Ce/Tl ratios with 2220 and 1840, respectively, which are higher than the depleted MORB mantle (DMM) range (1280±215, 1sd; Nielsen et al., 2014). The rest of the samples range between 37 and 603, with an average Ce/Tl ratio of 393.

The AVB lavas have ε^{205}Tl between -2.7 and +6.4, with an average value of +0.1. The lightest Tl signature is ε^{205}Tl = -2.7, which is indistinguishable from the upper mantle, as defined by MORB (-2±1; Nielsen et al., 2006a). Of the twenty samples measured, seven are isotopically heavier than the upper mantle. Four show positive ε^{205}Tl from 0 to +2, and three exhibit even heavier signatures between +4.3 and +6.4.

5.2 Sulfides in sample ASKL-3

Several sulfide grains are observed by SEM with diameters less than 20 μm (Fig. 5), and three of them are measured by EPMA (Table 3). These sulfides are all pyrite, with ~57 wt% iron (Fe), 39-40 wt% sulfur (S), and 2-3 wt% nickel (Ni). Lead concentrations of the pyrites are variable, from below the detection limit (100 μg/g) to 720 μg/g. Thallium concentration of the pyrites is below the detection limit of EPMA (200 μg/g).

6. Discussion

6.1 Source of Tl in K-rich lavas

The AVB lavas are characterized by elevated Tl concentrations, indicating a Tl-enriched source. Previous study suggests that the AVB lavas originate from a phlogopite-bearing peridotite source (Wei et al., 2017). Phlogopite is extremely enriched in Tl (up to ~12 μg/g; Brett et al., 2018; Rader et al., 2018; Fitzpayne et al., 2020), whereas Tl concentrations of olivine, pyroxene and spinel are below the detection limit (<1 ng/g) (Nielsen et al., 2014). Additionally, surface wave tomography has documented the existence of mica in the Tibetan mantle (Hacker et al., 2000, 2014) and phlogopite-peridotite mantle xenoliths are widely distributed in Tibetan post-collisional lavas (Luo et al., 2000; Zhao et al., 2008; Lai et al., 2011; Liu et al., 2011; Wang et al., 2016). Based on this evidence, we suggest that phlogopite is most likely the main host mineral for Tl in the source region of the AVB lavas.

Phlogopite is a hydrous mineral, which can buffer fluid compositions in the mantle (Frost, 2006). Therefore, phlogopite is often regarded as an indicator of metasomatism in the lithospheric mantle (Safonov et al., 2019), indicating the source region of the AVB lavas was previously metasomatized by fluids. This interpretation is also supported by their relatively low Ce/Tl ratios (Fig. 4), as fluids carry abundant Tl but very low Ce. Similarly, K-rich lavas in other post-collisional settings are also attributed to phlogopite-bearing sources in the lithospheric mantle (e.g., Condamine and Medard, 2014; Foley, 1992; Förster et al., 2018; Moghadam et al., 2018; Wang et al., 2020a, 2020b). Thallium preferentially substitutes for K in crystallographic textures (Heinrichs et al., 1980), resulting in Tl enrichment in K-rich lavas in post-collisional settings. Lavas from South Tibet and Anatolia exhibit enriched Tl concentrations as high as 1.68 and 0.44 μg/g, respectively (Moghadam et al., 2018; Wang, et al., 2020b). Moreover, melting experiments demonstrate that partial melting and breakdown of phlogopite can significantly increase the Rb/Sr ratios of melts (Förster et al., 2017). As shown in the Rb/Sr versus Tl plot (Fig. 6), Rb/Sr ratios correlate positively with Tl concentrations, indicating that phlogopite in the continental lithospheric mantle is likely the main source for Tl. Additionally, phlogopite is stable in the continental upper mantle down to 150-200 km (Kushiro et al., 1967) and the existence of fluorine (F) and Ti in

phlogopite can increase the stability of phlogopite (Motoyoshi and Hensen, 2001). In summary, phlogopite is not only an indicator of metasomatism, but also an important Tl host mineral in the continental lithospheric mantle.

Notably, Tl is not consistently enriched in K-rich volcanic rocks. Amphibole is also an important K-rich phase in the lithospheric mantle, but its Tl content is significantly variable. For example, in the absence of the phlogopite phase, orthomagmatic amphiboles generally contain Tl concentrations within the ng/g range, whereas late-magmatic to hydrothermal amphiboles have up to 3 μg/g Tl (Hettmann et al., 2014). Additionally, the amphibole/melt partition coefficient (0.04-0.23) is significantly lower than the phlogopite/melt partition coefficient (3.03-5.2) (Adam and Green, 2006). Therefore, K-rich lavas produced by melting of an amphibole-bearing source may contain variable Tl concentrations.

Partial melting modeling (see Appendix) suggests that the AVB lavas can be produced by 1-3% batch melting of phlogopite peridotite; therefore, Tl concentrations in the source region can be calculated by Tl concentrations of the most mafic samples. According to the D values for Tl ($D_{olivine\text{-}melt}$ = 0.01; $D_{orthopyroxene\text{-}melt}$ = 0.01; $D_{clinopyroxene\text{-}melt}$ = 0.01; $D_{garnet\text{-}melt}$ = 0.000001; $D_{phlogopite\text{-}melt}$ = 3.03) from Adam and Green (2006), in order to produce Tl concentrations of the most mafic lavas (ASKL-17, Tl concentration=0.290 μg/g; ASKL-18, Tl concentration=0.276 μg/g) by 1% batch melting, 44-46 ng/g of Tl in the source is required, whilst for 3% batch melting, 62-65 ng/g of Tl is required. Therefore, Tl concentrations in the sources can be estimated as a range of 44-65 ng/g, which is comparable to the Tl concentration of enriched peridotite xenoliths (12.9-85.7 ng/g; Chin et al., 2012).

6.2 Influence of secondary processes on Tl

It has been well documented that secondary processes like alteration, weathering, and degassing can potentially modify chemical and isotopic compositions of Tl in magmas (e.g., Nielsen et al., 2005, 2021; Baker et al., 2009; Prytulak et al., 2017). Therefore, these processes should be first evaluated before constraining the Tl characteristics in the mantle source. Although fractional crystallization of anhydrous

phases does not appear to fractionate Tl isotopes, we re-examine fractional crystallization processes in the AVB lavas, as they contain hydrous phases such as phlogopite.

6.2.1 Alteration and weathering

Alteration and weathering commonly influence the mobilization and re-distribution of elements in rocks, and can fractionate the isotopes of some elements during extreme weathering, e.g., lithium (Pistiner and Henderson, 2003). Measurements of Tl isotopes in variable continental sources suggest little fractionation of Tl isotopes during weathering and alteration processes (Nielsen et al., 2005), even when extreme weathering causing laterite formation is considered (Howarth et al. 2018). Due to the high solubility of alkali metals in aqueous solutions and similar geochemical properties between Tl and alkali metals, Rb and Tl are likely to decrease during subaerial alteration (Schiano et al., 1993; Babechuk et al., 2014). On the contrary, Th is immobile and preferentially hosted in resistant minerals even during extreme weathering (Ma et al., 2007). Approximate equal partition coefficient (D) values of Ce and Tl imply similar behaviors of these two elements during high-temperature magmatic processes and thus weathering and subaerial alteration can sometimes be identified by high Ce/Tl and Th/Rb ratios of lava samples.

As shown in Fig. 4, although the Ce/Tl ratios of sample ASKL-7 and 513-11 are significantly higher than the other samples and DMM (1280±215, 1sd; Nielsen et al., 2014), the Th/Rb ratios of these two samples are similar to the others, suggesting a negligible effect of subaerial alteration. Moreover, fresh petrology in thin sections and the leaching tests (Fig. 2) also do not support any obvious influence of subaerial alteration and weathering. Additionally, low loss on ignition (LOI) values (1.7% on average) and no correlation between Tl isotopes and LOI (not shown) also demonstrate negligible impacts of subaerial alteration and weathering on the AVB lavas.

6.2.2 Fractional crystallization and crustal assimilation

Fractional crystallization of magma is a key process to alter elemental

concentrations depending on their compatibilities in crystallizing phases. Correlations of elemental concentrations indicate that the AVB lavas experienced significant fractional crystallization during magmatic evolution (Wei et al., 2017). Thallium behaves as a highly incompatible lithophile element (e.g., Prytulak et al., 2017; Brett et al., 2021), and thus its concentration increases substantially during fractional crystallization. As shown in Fig.7a, except for two samples (ASKL-7 and 513-11) with low Tl concentrations coupled with heavy ε^{205}Tl and the sample with high Tl concentration (ASKL-3 = 8.2 μg/g, not shown), Tl concentrations are well correlated with MgO wt%, indicating a significant influence of fractional crystallization on Tl concentrations.

Fractional crystallization of anhydrous phases is not expected to cause Tl isotopic fractionation (Prytulak et al., 2017; Gaschnig et al. 2021). However, the Tl isotopic fractionation effects of hydrous minerals are much less well understood. Phlogopite is present in some of the AVB lavas (Table 1). Although data is currently limited, measurements of phlogopite separates from mantle xenoliths are indistinguishable from upper mantle values (ε^{205}Tl ~ -2.5; n=25; Fitzpayne et al. 2020), suggesting that partitioning of Tl into phlogopite does not induce a significant isotope fractionation. Moreover, no correlation of the occurrence of phlogopite and MgO content with Tl isotopes is observed in the AVB lavas (Fig. 7b). Based on these reasons, we suggest the impact of fractional crystallization on Tl isotope is insignificant.

Obvious crustal assimilation has been excluded by restricted radiogenic Sr and Nd isotopes of the AVB lavas in different ages (Wei et al., 2017). Due to the extremely high concentrations of Tl in the crust compared to that in the mantle, minor crustal assimilation can potentially alter the chemical and isotopic compositions of Tl in mantle-derived lavas, such as oceanic island basalt (e.g., Brett et al., 2021). However, the AVB lavas in this study originate from an incompatible element-enriched source, and thus the primitive magmas exhibit extremely high Tl concentrations. As shown in Table 1 and 2, the average Tl concentrations of the AVB lavas and the most primitive sample (ASKL-17) are 1.1 μg/g and 0.29 μg/g, respectively, which are within the concentration order of magnitude in the continental crust (~0.5 μg/g, Heinrichs et al.,

1980). Therefore, small proportions of crust are unlikely to significantly modify the Tl concentrations and isotopic composition of the AVB lavas.

Sample ASKL-3 has an extremely high Tl concentration of ~8.3 μg/g, whereas the remainder of the samples has Tl concentrations < 2 μg/g. Thallium behaves similarly with alkali metals, such as K, Cs, and Rb, and is commonly enriched in alkali-bearing minerals (Heinrichs et al., 1980). However, sample ASKL-3 does not have a distinctly high concentration of alkali metals compared to the other samples, excluding the possibility of contamination of alkali-bearing minerals, such as phlogopite. Moreover, no phlogopite phenocryst is observed in the thin section of ASKL-3, and samples with obvious phlogopite minerals do not show abnormally high Tl concentrations compared to the rest of the lavas, such as sample ASKL-16 (Tl = 0.76 μg/g).

Sulfides can be important Tl host minerals. In sample ASKL-3, there are several pyrite grains (Fig. 5), which have Pb concentrations as high as 720 μg/g (Table 3). Thallium behaves similarly with Pb in sulfides (Nielsen et al., 2014), and Tl is commonly enriched in pyrites (Vaněk et al., 2022). Therefore, although Tl is not detected by EPMA with a high detection limit of 200 μg/g, we speculate the pyrites in ASKL-3 have high Tl and Pb concentrations. This is also supported by the coupled elevated Pb and Tl contents of ASKL-3. Consequently, the abnormally high Tl concentration of ASKL-3 is likely attributable to contamination of Tl-bearing sulfides with relatively light Tl isotopic composition, which is consistent with our repeated digestion and measurement of Tl concentration of 7.2 μg/g, indicating uneven mixing of Tl-rich grains. Hence, we do not consider sample ASKL-3 further in the discussion of the source of the AVB lavas.

6.2.3 Kinetic fractionation of Tl isotopes by degassing

Owing to the relatively low boiling point of Tl (1453℃; Kaplan and Mattigod, 1998), enrichment of Tl in volcanic gases and mineralization of Tl sulfates in volcanic fumaroles have been reported by several studies (e.g., Baker et al., 2009; Siidra et al., 2014), suggesting that light isotope (^{203}Tl) is more likely to be lost during degassing. A recent magma degassing experiment revealed that 60-90% Tl was lost during magma

degassing, which caused significant kinetic isotope fractionation with heavier Tl isotope (^{205}Tl) remaining in residual melts (Nielsen et al., 2021). Given Ce and Tl behave similarly during high-temperature magmatic processes, but Tl is volatile whilst Ce (boiling point = 3257°C; Habermann and Danne, 1964) is not, volcanic degassing is predicted to result in relatively high Ce/Tl coupled with heavy Tl isotope ratios (Nielsen et al., 2016, 2017b). Under this framework, a significant influence of degassing on magmas has been identified in several volcanic areas, such as Central America, where the degassed volcanic rocks exhibit Tl isotopes as high as +9.0 ε-units (Nielsen et al., 2017a).

As shown in Fig. 4, two samples (ASKL-7 and 513-11) exhibit significantly higher Ce/Tl ratios and heavier Tl isotopic compositions than the others. Since the influence of subaerial alteration and weathering have been excluded in the above discussion, such heavy Tl isotopic values (+4.3 to +6.4) could be caused by addition of marine Fe-Mn sediments or volcanic degassing. However, the addition of marine Fe-Mn sediments will reduce the Ce/Tl ratios, which is opposite to the relatively high Ce/Tl ratios of ASKL-7 and 513-11 (Fig. 4). Therefore, we suggest that the heavy Tl isotopic signatures of ASKL-7 and 513-11 are likely due to kinetic fractionation during magma degassing. This Tl-loss process can also be identified in Fig. 7 that these two samples exhibit significantly lower Tl contents (148-154 ng/g) than the other samples (≥276 ng/g). In the Tl versus Rb diagram (Fig. 7d), sample ASKL-8 is plotted above the fitting line with relatively heavy Tl isotope (+1.9) and high Tl content (1960 ng/g), which may be related to the addition of marine Fe-Mn sediments in the source. Thallium concentrations of the other samples correlate well with MgO (Fig. 7a) and Rb (Fig. 7d), suggesting that the Tl budgets of these samples are not profoundly fractionated by degassing in the late stage of fractional crystallization.

The AVB lavas were produced by partial melting of phlogopite-bearing peridotite; therefore, their parental magma should be characterized by high concentrations of fluids. Degassing of the parental magma before fractional crystallization can potentially produce Tl isotopic fractionation. However, the most primitive sample (ASKL-17, MgO = 7.40%) exhibits a mantle-like ε^{205}Tl of -1.2, suggesting negligible Tl isotopic

fractionation. Degassing of the parental magma should produce higher Ce/Tl ratios and heavier Tl isotopes than ASKL-17 (Fig. 4b), which is inconsistent with the observation that except for sample 513-11 and ASKL-7, the Ce/Tl ratios of the remaining samples are close to or much lower than that of ASKL-17. Consequently, based on these lines of evidence, we suggest that the Tl isotopes of the parental magma were not significantly fractionated by degassing.

To roughly quantify the impacts of degassing on sample ASKL-7 and 513-11, a simple calculation is performed: assuming Tl concentrations of these two samples were well correlated with Rb as the other samples before degassing. The fitting line of Tl versus Rb is Tl = 0.0085*Rb - 0.3819 (R^2 = 0.81) (Fig. 7d), and thus the Tl concentrations of ASKL-7 and 513-11 before degassing can be calculated by their Rb concentrations as 0.57 and 1.28 μg/g, respectively. As a result, loss of Tl for sample ASKL-7 and 513-11 can be calculated as 74% and 88%, respectively. This result is consistent with the degassing experiment that indicated 60-90% Tl loss (Nielsen et al., 2021).

Loss of volcanic gas (mainly water) can increase the melt viscosity and density, and expedite fractional crystallization due to undercooling of the melt (Sparks, 2003). Sample ASKL-7 and 513-11 were collected at Yueya and Yizi volcanoes in the AVB, respectively. These two volcanoes have the smallest terraces in length (Xu et al., 2012), which may be related to the relatively high viscosity of magma caused by degassing. However, these two degassed samples show no anomalies in petrography compared with other samples, probably because crystallization and vesicles are controlled by many factors. In this study, although degassing of volcanic rocks is common as recorded by vesicles, only two samples have been identified that likely experienced significant Tl degassing. Therefore, we suggest that kinetic fractionation of Tl isotopes by degassing does not significantly affect the rest of the samples, which do not display high Ce/Tl coupled with heavy Tl isotopic compositions.

6.3 Identifying enriched components in the source

Excepting sample ASKL-3 (possible sulfides) and the two degassed samples

(ASKL-7 and 513-11), the remaining 17 AVB samples exhibit variable ε^{205}Tl ranging from -2.0 to +5.1, of which 9 samples are heavier than the depleted upper mantle (-2±1). As documented above, secondary processes cannot account for these heavy Tl isotopic variations, indicating that the mantle source also contains heavy Tl. By combining geochemical and geophysical observations, our previous study has proposed that the AVB lavas were produced by partial melting of a previously metasomatized source in the SCLM (Wei et al., 2017). Partial melting and mantle metasomatism at mantle temperature (T) are unlikely to fractionate Tl isotope to an analytically resolvable level (Nielsen et al., 2017; Prytulak et al., 2017) because the magnitude of Tl isotopic fractionation is proportional to $1/T^2$ (Bigeleisen and Mayer, 1947; Urey, 1947). Additionally, phlogopite in MARID xenoliths from South Africa exhibits an overlapped Tl isotopic range (-2.5±1.3, 2sd; Fitzpayne et al., 2020) with the depleted mantle (-2.0±1.0; Nielsen et al., 2017b), also indicating that high-temperature partial melting and mantle metasomatism associated with phlogopite may not cause profound Tl isotopic fractionation. In conclusion, mantle metasomatism and partial melting of phlogopite peridotite are unlikely to account for the Tl isotopic variations of the AVB lavas, and the Tl isotopic variations should be attributed to the enriched components in the source.

Enriched Sr-Nd isotopic compositions of the AVB lavas indicate the existence of enriched mantle II (EM II) components in their mantle source (Wei et al., 2017), but where it was inherited is unclear. Continental sediments have similar ε^{205}Tl values (-2±1; Nielsen et al., 2005, 2017b) to the depleted mantle (-2±1; Nielsen et al., 2017b), and therefore mixing them cannot produce the AVB lavas with variable Tl isotopes (-2.0 to +5.1). Oceanic sediments commonly retain substantial Tl isotopic variations and high Tl concentrations (e.g., Nielsen et al., 2016; 2017b). Consequently, the large range of Tl isotope of the AVB lavas should be attributed to oceanic enriched components. The addition of continental material cannot be ruled out through Tl isotope because continental sediments have overlapped ε^{205}Tl value (-2±1; Nielsen et al., 2005, 2017b) with the AVB lavas (-2.0 to +5.1), as well as with the depleted mantle (-2.0±1.0 2sd; Nielsen et al., 2017b). However, if the enriched contributions from the southward-subducting continental Tarim block are dominant, the Pulu volcanoes on the north of

510 the AVB should have more enriched Sr-Nd isotopic compositions than the AVB lavas,
511 which is opposite to the observations (Wang et al., 2020a). Based on these reasons, we
512 believe that oceanic components play a dominant role in the enrichment in the mantle
513 source of the AVB lavas. To clarify the contribution of continental sediments, future Tl
514 isotopic investigations on K-rich post-collisional lavas and mantle xenoliths in the
515 surrounding areas are needed.

516 Notably, the AVB lavas have restricted Sr and Nd isotopes but variable Tl isotopes,
517 and therefore a clear decoupling of radiogenic and stable isotope systems is apparent in
518 these lavas. This scenario can be explained by the great Tl concentration contrast
519 between the depleted mantle and oceanic inputs; therefore, minor addition of oceanic
520 high-Tl materials will dominate both the chemical and isotopic Tl budget of lavas. For
521 example, ferromanganese (Fe-Mn) nodules retain extremely high Tl concentrations
522 (100 μg/g) and enriched Tl isotopes ($\varepsilon^{205}Tl > +10$) (Nielsen et al., 2006a). Binary
523 mixing calculations indicate that addition of 0.2% Fe-Mn nodules cannot sufficiently
524 modify the Sr and Nd isotopes of the mantle, but can significantly change their Tl
525 isotope from -2 to +7.1. As shown in Fig. 8, none of the AVB samples exhibit lower
526 $\varepsilon^{205}Tl$ than the upper mantle range (-2±1), indicating that the addition of low-T altered
527 oceanic crust ($\varepsilon^{205}Tl < -5$) is minor or overprinted by high-Tl pelagic or Fe-Mn
528 sediments. Hence, heterogeneous addition of sufficient oceanic sediments can account
529 for the variable Tl isotopic but restricted Sr-Nd isotopic compositions.
530
531 **6.4 Tethys Oceanic contributions to post-collisional K-rich magmatism on Tibet**
532 Apart from Tl isotope systematics in northern Tibet, oceanic components have also
533 been identified in southern and eastern Tibet through other stable isotopes such as Mg,
534 Ca, and Os isotopes (Liu et al., 2015; Liu et al., 2017). Before the Indian-Asian collision,
535 the lithosphere of Tibet experienced a long history of Paleo-Tethys and subsequent Neo-
536 Tethys oceanic subductions, which can be evidenced by the west-east sutures on Tibetan
537 Plateau (Wu et al., 2020). As shown in Fig. 1, KS and JS sutures in north Tibet mark
538 the closure of Paleo-Tethys Ocean within Paleozoic, whereas BNS and ITS sutures in
539 south Tibet indicate the closure of Neo-Tethys Ocean mainly in Mesozoic (Wu et al.,

2020). Middle Triassic granitoids in NW Tibet retain similar Sr-Nd isotopes and high K content with the AVB lavas (Jiang et al., 2013), also supporting the connection between Paleo-Tethys oceanic subductions and post-collision lavas herein. Additionally, chemical and Sr-Nd isotopic compositions of Cenozoic mafic rocks in Lhasa Terrane are similar to those of Cretaceous subduction-related magmatism in southern Tibet, demonstrating the sustained influence of the Neo-Tethys Ocean slab on the post-collisional lavas in Tibet (Huang et al., 2020). Additionally, average Nd and Pb model ages for the post-collisional basalts in Tibet are 0.9-1.3 and 2.2-3.5 Ga, respectively (Turner et al., 1996). Therefore, based on these lines of evidence, we propose that the enriched K-rich components in Tibetan post-collisional lavas are mainly attributed to multi-stage Paleo- and Neo-Tethys subductions.

Combined with these geological and geochemical constraints, a two-stage geodynamic model is proposed in Fig. 9. Before the Indian-Asian collision, the Tibetan lithosphere was metasomatized by high-K components from Paleo- and Neo-Tethys Oceanic subductions, and may form phlogopite peridotite veins in the lithospheric mantle (Wang et al., 2014). Subsequently, due to the Indian-Asian collision and continuous underthrusting of the Indian Plate beneath the Tibetan Plateau, a series of complex geodynamic processes occurred on the Tibetan Plateau. These geodynamic processes, including convective thinning, delamination, slab roll-back and break-off, and shear heating, may induce partial melting of the metasomatized mantle and form a large amount of west-east extension of post-collisional magmatism belts in Tibet.

7. Conclusion

Thallium isotopic compositions have been applied as a source tracer for about two decades. Most studies on Tl isotopes focus on arc or OIB-related magmatism and the mechanisms responsible for Tl isotopic fractionations are still not fully understood. We measured Tl isotopes of K-rich lavas in post-collisional settings. Significantly fractionated Tl isotopes are found, however, there appears to be a clear role for kinetic fractionation in producing some of the isotopically heavy signatures. After evaluating the influence of subaerial alteration, degassing, fractional crystallization, and crustal

assimilation on Tl isotope fractionation, we suggest the remaining heavy signatures originated from the source. Significant variations in Tl isotopes suggest contributions of oceanic sediments, which documents that the enriched components in Cenozoic Tibet lavas may originate from Paleo- and Neo-Tethys components stored in the SCLM.

By conducting batch melting modeling, we suggest the AVB lavas were produced by 1-3% partial melting of phlogopite-peridotite. Phlogopite is not only an indicator of metasomatism but also an important host mineral for Tl. We also estimate the Tl concentration in the source region as 44-65 ng/g, which is comparable to the Tl concentration of enriched peridotite xenoliths. We suggest metasomatism in the source does not fractionate Tl isotopes significantly and the Tl isotopic variations in the source are invoked to heterogeneous addition of sufficient high-Tl oceanic materials. Finally, we proposed a two-stage model that previously metasomatized SCLM by Paleo- and Neo-Tethys Ocean components are responsible for the wide distribution of K-rich post-collisional lavas on the Tibetan Plateau.

Acknowledgments

We thank the editor Dr. Sonja Aulbach and two anonymous reviewers for their constructive comments and suggestions that helped us greatly improve the manuscript. This work was funded by the Fundamental Research Funds in the Institute of Geology, China Earthquake Administration (Grant IGCEA1904), National Natural Science Foundation of China (Grant 41372344), a China Scholarship Council award (Grant 201504190007) to FW for his visit to the MAGIC Laboratories at Imperial College London, and Undergraduate Research Opportunity internship to EBB (Imperial College London). We would like to greatly thank B. Coles and K. Kressig from the MAGIC and S.Hammond from Open University for the mass spectrometry and chemistry.

References

Adam, J., Green, T., 2006. Trace element partitioning between mica- and amphibole-bearing garnet lherzolite and hydrous basanitic melt: 1. Experimental results and the investigation of controls on partitioning behaviour. Contrib. Mineral. Petrol. 152, 1-17.

Babechuk, M.G., Widdowson, M., Kamber, B.S., 2014. Quantifying chemical weathering intensity and trace element release from two contrasting basalt profiles, Deccan Traps, India. Chem. Geol. 363, 56-75.

Baker, R.G.A., Rehkämper, M., Hinkley, T.K., Nielsen, S.G., Toutain, J.P., 2009. Investigation of thallium fluxes from subaerial volcanism- Implications for the present and past mass balance of thallium in the oceans. Geochim. Cosmochim. Acta 73, 6340-6359.

Bigeleisen, J., Mayer, M. G., 1947. Calculation of equilibrium constants for isotopic exchange reactions. J. Chem. Phys. 15(5), 261-267.

Blusztajn, J., Nielsen, S.G., Marschall, H.R., Shu, Y., Ostrander, C., Hanyu, T., 2018. Thallium isotope systematics in volcanic rocks from St. Helena – constraints on the origin of the HIMU reservoir. Chem. Geol. 476, 292-301.

Brett, A., Prytulak, J., Hammond, S.J., Rehkämper, M., 2018. Thallium isotope ratio and mass fraction of sixteen reference materials. Geostand. Geoanal. Res. 42(3), 339-360.

Brett, E.K.A., Prytulak, J., Rehkämper, M., Hammond, S.J., Chauvel, C., Stracke, A., Willbold, M., 2021. Thallium elemental and isotopic systematics in ocean island lavas. Geochim. Cosmochim. Acta 301, 187-210.

Chin, E.J., Lee, C.A., Luffi, P., Tice, M., 2012. Deep lithospheric thickening and refertilization beneath continental arcs: Case study of the P, T and compositional evolution of peridotite xenoliths from the Sierra Nevada, California. J. Petro. 53(3), 477-511.

Chung, S.L., Chu, M.F., Zhang, Y., Xie, Y., Xie, Y., Lo, C.H., Lee, T.Y., Lan, C.Y., Li, X., Zhang, Q., Wang, Y., 2005. Tibetan tectonic evolution inferred from spatial and temporal variation in post-collisional magmatism. Earth Sci. Rev. 68, 173–196.

Condamine, P., Médard, E., 2014. Experimental melting of phlogopite-bearing mantle at 1 GPa: Implications for potassic magmatism. Earth Planet. Sci. Lett. 397, 80-92.

Condamine, P., Médard, E., Devidal., J., 2016. Experimental melting of phlogopite-peridotite in the garnet stability field. Contrib. Mineral. Petrol. 171, 95.

Ding, L., Kapp, P., Zhong, D., Deng, W., 2003. Cenozoic volcanism in Tibet: evidence for a transition from oceanic to continental subduction. J. Petrol. 44 (10), 1833–1865.

Downes, H., Kostoula, T., Jones, A. P., Beard, A., Thirlwall, M. F., Bodinier, J. 2002. Geochemistry and Sr-Nd isotopic compositions of mantle xenoliths from the Monte Vulture carbonatite-melilitite volcano, central southern Italy. Contrib. Mineral. Petrol. 144(1), 78-92.

Fitzpayne, A., Prytulak, J., Giuliani, A., Hergt, J., 2020. Thallium isotopic composition of phlogopite in kimberlite-hosted MARID and PIC mantle xenoliths. Chem. Geo. 531, 119347.

Foley, S., 1992. Vein-plus-wall-rock melting mechanisms in the lithosphere and the origin of potassic alkaline magmas. Lithos 28, 435-453.

Förster, M.W., Prelević, D., Schmück, H.R., Buhre, S., Veter, M., Mertz-Kraus, R., Foley, S.F., Jacob, D.E., 2017. Melting and dynamic metasomatism of mixed harzburgite + glimmerite mantle source: Implications for the genesis of orogenic potassic magmas. Chem. Geol. 455, 182-191.

Förster, M.W., Prelević, D., Schmück, H.R., Buhre, S., 2018. Melting phlogopite-rich MARID: Lamproites and the role of alkalis in olivine-liquid Ni-partitioning. Chem. Geol. 476, 429-440.

Frost, D.J., 2006. The Stability of Hydrous Mantle Phases. Reviews in Mineralogy and Geochemistry 62(1), 243-271.

Gaschnig, R.M., Rader, S.T., Reinhard, C.T., Owens, J.D., Planavsky, N., Wang, X., Asael, D., Greaney, A., Helz, R., 2021. Behaviour of the Mo, Tl, and U isotope systems during differentiation in the Kilauea Iki lava lake. Chem. Geol. 574, 120239.

Genna, D., Gaboury, D., 2015. Deciphering the hydrothermal evolution of a VMS system by LA-ICP-MS using trace elements in pyrite: an example from the Bracemac-McLeod deposits, Abitibi, Canada, and implications for exploration. Econ. Geol. 110(8), 2087-2108.

Guo, Z., Wilson, M., Zhang, L., Zhang, M., Cheng, Z., Liu, J., 2014. The role of subduction channel mélanges and convergent subduction systems in the petrogenesis of postcollisional K-rich mafic magmatism in NW Tibet. Lithos 198-199, 184–201.

Guo, Z., Wilson, M., 2019. Late Oligocene-early Miocene transformation of postcollisional magmatism in Tibet. Geology 47(8), 776-780.

Habermann, C.E., Daane, A.H., 1964. Vapor pressures of the rare- earth metals. J.

688 Chem. Phys. 41(9), 2818-2827.
689
690 Hacker, B. R., Gnos, E., Ratschbacher, L., Grove, M., Mcwilliams, M., Sobolev, S.V.,
691 Wang, J., Zhenhan, W. 2000. Hot and Dry Deep Crustal Xenoliths from Tibet. Science
692 287(5462), 2463-2466.
693
694 Hacker, B.R., Ritzwoller, M.H., Xie, J., 2014. Partially melted, mica-bearing crust in
695 Central Tibet. Tectonics 33, 1408-1424.
696
697 Heinrichs, H., Schulz-Dobrich, B., Wedepohl, K.H., 1980. Terrestrial geochemistry of
698 Cd, Bi, Tl, Pb, Zn and Rb. Geochim. Cosmochim. Acta 44, 1519-1533.
699
700 Hettmann, K., Marks, M.A., Kreissig, K., Zack, T., Wenzel, T., Rehkämper, M., Jacob,
701 D.E., Markl, G., 2014. The geochemistry of Tl and its isotopes during magmatic and
702 hydrothermal processes: The peralkaline Ilimaussaq complex, southwest Greenland.
703 Chem. Geol., 366, 1-13.
704
705 Howarth, S., Prytulak, J., Little, S.H., Hammond, S.J., Widdowson, M., 2018. Thallium
706 concentration and thallium isotope composition of lateritic terrains. Geochim.
707 Cosmochim. Acta 239, 446-462.
708
709 Huang, F., Rooney, T.O., Xu, J.F., Zeng, Y.C., 2020. Magmatic record of continuous
710 Neo-Tethyan subduction after initial India-Asia collision in the central part of southern
711 Tibet. GSA Bulletin 133(7-8), 1600-1612.
712
713 Jenner, F.E., O'Neill, H.S.C. 2012. Analysis of 60 elements in 616 ocean floor basaltic
714 glasses. Geochem. Geophys. Geosyst. 13(2), doi: 10.1029/2011GC004009.
715
716 Jiang, Y.H., Jia, R.Y., Liu, Z., Liao, S.Y., Zhao, P., Zhou, Q., 2013. Origin of Middle
717 Triassic high-K calc-alkaline granitoids and their potassic microgranular enclaves from

718 the western Kunlun orogen, northwest China: A record of the closure of Paleo-Tethys.
719 Lithos 156-159, 13-30.
720
721 Kaplan, D.I., Mattigod, S.V., 1998. Aqueous geochemistry of thallium. Advances in
722 Environmental Science and Technology- New York 29, 15-30.
723
724 Kushiro, I., Syono, Y., Akimoto, S., 1967. Stability of phlogopite at high pressures and
725 possible presence of phlogopite in the earth's upper mantle. Earth Planet. Sci. Lett.
726 3,197-203.
727
728 Lai, S., Qin, J., Grapes, R., 2011. Petrochemistry of granulite xenoliths from the
729 Cenozoic Qiangtang volcanic field, northern Tibetan Plateau: implications for the lower
730 crust composition and genesis of the volcanism. Int. Geol. Rev. 53(8), 926-945.
731
732 Liu, C., Wu, F., Chung, S., Zhao, Z., 2011. Fragments of hot and metasomatized mantle
733 lithosphere in Middle Miocene ultrapotassic lavas, southern Tibet. Geology 39(10),
734 923-926.
735
736 Liu, F., Li, X., Wang, G., Liu, Y., Zhu, H., Kang, J., Huang, F., Sun, W., Xia, X., Zhang,
737 Z., 2017. Marine Carbonate Component in the Mantle Beneath the Southeastern
738 Tibetan Plateau: Evidence From Magnesium and Calcium Isotopes. J. Geophys. Res.:
739 Solid Earth 122(12), 9729-9744.
740
741 Liu, J., Maimaiti, Y., 1989. Distribution and ages of Ashikule volcanoes on the west
742 Kunlun mountains, west China. Bull. Glacial Res. 7, 187–190.
743
744 Liu, J.Q., Ren, Z.Y., Nichols, A.R., Song, M.-S., Qian, S.P., Zhang, Y., Zhao, P.P.,
745 2015. Petrogenesis of Late Cenozoic basalts from North Hainan Island: Constraints
746 from melt inclusions and their host olivines. Geochim. Cosmochim. Acta 152, 89-121.
747

748 Luo, Z., Zhang, W., Deng, J., Zheng, J., Su, S., 2000. Characteristic and geological
749 significance of the deep-seated xenoliths in Cenozoic basalt in Kangxiwa, Western
750 Kunlun Mountains, China. Earth Sci. Front. 7(1), 295-298 (in Chinese with English
751 Abstract).
752
753 Ma, J., Wei, G., Xu, Y., Long, W., Sun, W., 2007. Mobilization and re-distribution of
754 major and trace elements during extreme weathering of basalt in Hainan Island, South
755 China. Geochim. Cosmochim. Acta 71, 3223-3237.
756
757 McDonough, W.F., Sun, S.S. 1995. The composition of the Earth. Chem. Geol. 120(3-
758 4), 223-253.
759
760 Moghadam S.H., Griffin, W.L., Kirchenbaur, M., Garbe-Schönberg, D., Zakie Khedr,
761 M., Kimura, J.I., Stern, R.J., Ghorbani, G., Murphy, R., O'Reilly, S.Y., Arai, S.,
762 Maghdour-Mashhour, R., 2018. Roll-Back, Extension and Mantle Upwelling Triggered
763 Eocene Potassic Magmatism in NW Iran. J. Petrol. 59(7), 1417-1465.
764
765 Motoyoshi, Y., Hensen, B.J., 2001. F-rich phlogopite in the ultra-high-temperature
766 metapelites from the Napier Complex, East Antarctica. Am. Mineral. 86, 1404-1413.
767
768 Nielsen, S.G., Mar-Gerrison, S., Gannoun, A., LaRowe, D., Klemm, V., Halliday, A.N.,
769 Burton, K.W. and Hein, J.R., 2009. Thallium isotope evidence for a permanent increase
770 in marine organic carbon export in the early Eocene. Earth Planet. Sci. Lett. 278(3-4),
771 297-307.
772
773 Nielsen, S.G., Rehkämper, M., Baker, J., Halliday, A.N., 2004. The precise and
774 accurate determination of thallium isotope compositions and concentrations for water
775 samples by MC-ICPMS. Chem. Geol. 204(1-2), 109-124.
776
777 Nielsen, S.G., Rehkämper, M., Porcelli, D., Andersson, P., Halliday, A.N., Swarzenski,

778 P.W., Latkoczy, C. and Günther, D., 2005. Thallium isotope composition of the upper
779 continental crust and rivers—An investigation of the continental sources of dissolved
780 marine thallium. Geochim. Cosmochim. Acta 69(8), 2007-2019.
781
782 Nielsen, S.G., Rehkämper, M., Norman, M.D., Halliday, A.N., Harrison, D., 2006a.
783 Thallium isotopic evidence for ferromanganese sediments in the mantle source of
784 Hawaiian basalts. Nature 439(7074), 314.
785
786 Nielsen, S.G., Rehkämper, M., Teagle, D.A., Butterfield, D.A., Alt, J.C., Halliday, A.N.,
787 2006b. Hydrothermal fluid fluxes calculated from the isotopic mass balance of thallium
788 in the ocean crust. Earth Planet. Sci. Lett. 251(1-2), 120-133.
789
790 Nielsen, S.G., Rehkämper, M., Brandon, A.D., Norman, M.D., Turner, S. and O'Reilly,
791 S.Y., 2007. Thallium isotopes in Iceland and Azores lavas—implications for the role
792 of altered crust and mantle geochemistry. Earth Planet. Sci. Lett. 264(1-2), 332-345.
793
794 Nielsen, S.G., Shimizu, N., Lee, C.A., Behn, M.D., 2014. Chalcophile behavior of
795 thallium during MORB melting and implications for the sulfur content of the mantle.
796 Geochem. Geophys. Geosyst. 15, 4905-4919.
797
798 Nielsen. S.G., Yogodzinski, G., Prytulak, J., Plank, T., Kay, S.M., Kay, R.W., Blusztajn,
799 J., Owens, J.D., Auro, M., Kading, T., 2016. Tracking along-arc sediment inputs to the
800 Aleutian arc using thallium isotopes. Geochim. Cosmochim. Acta 181, 217-237.
801
802 Nielsen, S.G., Prytulak, J., Blusztajn, J., Shu, Y., Auro, M., Regelous, M., Walker, J.,
803 2017a. Thallium isotopes as tracers of recycled materials in subduction zones: Review
804 and new data for lavas from Tonga-Kermadec and Central America. J. Volcanol.
805 Geotherm. Res. 339, 23-40.
806
807 Nielsen, S.G., Rehkämper, M., Prytulak, J., 2017b. Investigation and Application of

Thallium Isotope Fractionation. Rev. Mineral. Geochem. 82(1), 759-798.

Nielsen, S.G., Shu, Y., Wood, B.J., Blusztajn, J., Auro, M., Norris, C.A., Wörner, G., 2021. Thallium isotope fractionation during magma degassing: evidence from experiments and Kamchatka Arc lavas. Geochem. Geophys. Geosyst. 22(5), e2020GC009608.

Peacock, C.L., Moon, E.M., 2012. Oxidative scavenging of thallium by birnessite: Controls on thallium sorption andstable isotope fractionation in marine ferromanganese precipitates. Geochim. Cosmochim. Acta 84, 297–313.

Pistiner J.S., Henderson, G.M. 2003. Lithium-isotope fractionation during continental weathering processes. Earth Planet. Sci. Lett., 214(1-2), 327-339.

Prytulak, J., Nielsen, S.G., Plank, T., Barker, M., Elliott, T., 2013. Assessing the utility of thallium and thallium isotopes for tracing subduction zone inputs to the Mariana arc. Chem. Geol. 345, 139-149.

Prytulak, J., Brett, A., Webb, M., Plank, T., Rehkämper, M., Savage, P.S., Woodhead, J., 2017. Thallium elemental behavior and stable isotope fractionation during magmatic processes. Chem. Geol. 448, 71-83.

Rader, S.T., Mazdab, F.K., Barton, M.D. 2018. Mineralogical thallium geochemistry and isotope variations from igneous, metamorphic, and metasomatic systems. Geochim. Cosmochim. Acta 243, 42-65.

Rehkämper, M. and Halliday, A.N., 1999. The precise of measurement of Tl isotopic compositions by MC-ICPMS: Application to the analysis of geological materials and meteorites. Geochim. Cosmochim. Acta 63(6), 935-944.

838 Rehkämper, M., Frank, M., Hein, J.R., Porcelli, D., Halliday, A., Ingri, J., Liebetrau, V.,
839 2002. Thallium isotope variations in seawater and hydrogenetic, diagenetic, and
840 hydrothermal ferromanganese deposits. Earth Planet. Sci. Lett. 197, 65–81.
841
842 Safonov, O., Butvina, V., Limanov, E., 2019. Phlogopite-Forming Reactions as
843 Indicators of Metasomatism in the Lithospheric Mantle. Minerals 9(11), 685.
844
845 Schauble, E.A., 2007. Role of nuclear volume in driving equilibrium stable isotope
846 fractionation of mercury, thallium, and other very heavy elements. Geochim.
847 Cosmochim. Acta 71(9), 2170-2189.
848
849 Schiano, P., Dupre, B., Lewin, E., 1993. Application of element concentration
850 variability to the study of basalt alteration (fangataufa atoll, French Polynesia). Chem.
851 Geol. 104, 99-124.
852
853 Shaw, D.M., 1952. The geochemistry of thallium. Geochim. Cosmochim. Acta 2, 118–
854 154.
855
856 Shu, Y., Nielsen, S.G., Zeng, Z., Shinjo, R., Blusztajn, J., Wang, X., Chen, S., 2017.
857 Tracing subducted sediment inputs to the Ryukyu arc-Okinawa Trough system:
858 Evidence from thallium isotopes. Geochim. Cosmochim. Acta 217, 462-491.
859
860 Shu, Y., Nielsen, S.G., Marschall, H.R., John, T., Blusztajn, J., Auro, M., 2019. Closing
861 the loop: subducted eclogites match thallium isotope composition of ocean island
862 basalts. Geochim. Cosmochim. Acta 250, 130-148.
863
864 Shu, Y., Nielsen, S.G., Le Roux, V., Blusztajn, J., Guo, S., Huang, F., 2022. Thallium
865 isotope compositions of subduction-zone fluids: insights from ultra-high pressure
866 eclogites and veins in the Dabie terrane, eastern China. Chem. Geol. 599, 120843.
867

Siidra, O.I., Vergasova, L.P., Krivovichev, S.V., Kretser, Y.L., Zaitsev, A.N., Filatov, S.K. 2014. Unique thallium mineralization in the fumaroles of Tolbachik volcano, Kamchatka Peninsula, Russia. I. Markhininite, $TlBi(SO_4)_2$. Mineral. Mag. 78(7), 1687-1698.

Sparks, R.S.J., 2003. Dynamics of magma degassing. Geological Society, London, Special Publications, 213(1), 5-22.

Tapponnier, P., Zhiqin, X., Roger, F., Meyer, B., Arnaud, N., Wittlinger, G., Jingsui, Y., 2001. Oblique stepwise rise and growth of the Tibet Plateau. Science 294, 1671–1677.

Turner, S., Arnaud, N., Liu, J., Rogers, N., Hawkesworth, C., Harris, N., Kelley, S., Van Clasteren, P., Deng, W., 1996. Post-collision, shoshonitic volcanism on the Tibetan Plateau: Implications for convective thinning of the lithosphere and the source of ocean island basalts. J. Petrol. 37(1), 45-71.

Turner, S., Hawkesworth, C., Liu, J., Rogers, N., Kelley, S., Calsteren, P.V., 1993. Timing of Tibetan uplift constrained by analysis of volcanic rocks. Nature 364(6432), 50-54.

Urey, H.C., 1947. The thermodynamic properties of isotopic substances. J. Chem. Soc. (Resumed), 562.

Vaněk, A., Vejvodová, K., Mihaljevič, M., Ettler, V., Trubač, J., Vaňková, M., Teper, L., Cabala, J., Sutkowska, K., Voegelin, A., Göttlicher, J., 2022. Evaluation of thallium isotopic fractionation during the metallurgical processing of sulfides: An update. J. Hazard. Mater. 424, 127325.

Wang, B., Chen, J., Xu, J., Wang, L., 2014. Geochemical and Sr–Nd–Pb–Os isotopic compositions of Miocene ultrapotassic rocks in southern Tibet: Petrogenesis and

implications for the regional tectonic history. Lithos 208-209, 237-250.

Wang, P., Zhao, G., Han, Y., Liu, Q., Zhou, N., Yao, J., Li, J., Li, Y., 2020a. Post-collisional potassic rocks in Western Kunlun, NW Tibet Plateau: Insights into lateral variations in the crust-mantle structure beneath the India-Asia collision zone. Lithos 370-371, 105645.

Wang, Z., Zhao, Z., Asimow, P.D., Liu, D., Zhu, D.-C., Mo, X., Wang, Q., Zhang, L., Sheikh, L., 2020b. Shoshonitic enclaves in the high Sr/Y Nyemo pluton, southern Tibet: Implications for Oligocene magma mixing and the onset of extension of the southern Lhasa terrane. Lithos 362-363, 105490.

Wang, R., Collins, W.J., Weinberg, R.F., Li, J., Li, Q., He, W., Richards, J.P., Hou, Z., Z, L., Stern, R.A., 2016. Xenoliths in ultrapotassic volcanic rocks in the Lhasa block: direct evidence for crust-mantle mixing and metamorphism in the deep crust. Contrib. Mineral. Petrol. 172, 62.

Wedepohl, K.H., 1974. Handbook of Geochemistry. Springer.

Wei, F., Prytulak, J., Xu, J., Wei, W., Hammond, O.S.J., Zhao, B., 2017. The cause and source of melting for the most recent volcanism in Tibet: A combined geochemical and geophysical perspective. Lithos 288-289, 175-190.

Weis, D., Frey, F.A., 1991. Isotope geochemistry of the Ninetyeast Ridge basement basalts: Sr, Nd, and Pb evidence for involvement of the Kerguelen hot spot. Proc. Ocean Drill Program Sci. Results 121, 591-610.

Weis, D., Frey, F.A., 1996. Role of the Kerguelan Plume in generating the eastern India Ocean seafloor. J. Geophys. Res.: Solid Earth 101(B6), 13831-13849.

928 Williams, H.M., Turner, S.P., Pearce, J.A., Kelley, S.P., Harris, N.B.W., 2004. Nature
929 of the source regions for post-collisional, potassic magmatism in southern and northern
930 Tibet from geochemical variations and inverse trace element modelling. J. Petrol. 45(3),
931 555-607.
932
933 Williamson, N.M.B., Weis, D., Prytulak, J. 2021. Thallium isotopic compositions in
934 Hawaiian lavas: evidence for recycled materials on the Kea side of the Hawaiian mantle
935 plume. Geochem. Geophys. Geosys. 22(9), e2021GC009765.
936
937 Wu, F., Wan, B., Zhao, L., Xiao, W., Zhu, R., 2020. Tethyan geodynamics. Acta Petrol.
938 Sin. 36(6), 1627-1674.
939
940 Xu, J., Zhao, B., Zhang, L., Chen, Z., 2012. Field geological exploration of the Ashikule
941 volcano Group in Western Kunlun Mountains. Earthquake Research in China 26(2),
942 152–159.
943
944 Xu, J., Zhao, B., Sindney, H., Chen, Z.Q., Zhang, L.Y., 2014. Geological features and
945 eruption history of Ashikule volcano clusters in western Kunlun Mountain. Acta Petrol.
946 Sin. 30(12), 3521-3520 (in Chinese with English Abstract).
947
948 Yin, A., Harrison, T.M., 2000. Geologic evolution of the Himalayan-Tibetan orogen.
949 Annual review of earth and planetary sciences 28(1), 211-280.
950
951 Yuan, Y., Zhong, Y., Guo, F., Xia, B., Zhang, Y., 2020. Geochemical and
952 geochronological constraints on the genesis of Pliocene post-collisional granite
953 porphyry and shoshonite in Quanshuigou, western Kunlun Mountains, NW Qinghai–
954 Tibet Plateau. Int. Geol. Rev., 64(2), 275-296.
955
956 Zhao, Z., Mo, X., Sun, C., Zhu, D., Niu, Y., Dong, Y., Dong, G., Zhou, S., Dong, X,
957 Liu, Y., 2008. Mantle xenoliths in southern Tibet: geochemistry and constraints for the

nature of the mantle. Acta Petrol. Sin. 24(2), 193-202 (in Chinese with English Abstract).

Appendix: Melting processes for the K-rich magmas

To constrain the partial melting degrees and verify that the trace element characteristics of the AVB lavas are produced by phlogopite-bearing peridotite, we performed trace-element modeling for batch melting of phlogopite-peridotite. The mineral assemblages of phlogopite peridotites can be constrained by xenoliths entrained in post-collisional K-rich lavas. Although no mantle xenolith has been found in the AVB, mantle xenoliths entrained in similar post-collisional K-rich lavas in northern Tibet are mainly phlogopite peridotite composed of olivine, orthopyroxene, clinopyroxene, garnet, spinel, and phlogopite (Liu et al., 2011; Luo et al., 2000; Zhao et al., 2008). Spinel, however, would cause variable Zr/Hf ratios, which is not observed in the AVB lavas (Wei et al., 2017). Thus, the mineral assemblages of peridotites beneath the AVB can be assumed as olivine, orthopyroxene, clinopyroxene, garnet, and phlogopite.

Since no trace element data of phlogopite-bearing peridotite in northwest Tibet has been reported, a mica-bearing peridotite xenolith from Monte Vulture in southern Italy (sample Aj33L, Downes et al., 2002), which displays similar source characteristics with the AVB lavas, is selected as the composition of mantle source. As demonstrated by melting experiments, partial melting of phlogopite-peridotite may follow the reaction: 0.59 phlogopite + 0.52 clinopyroxene + 0.18 garnet = 0.06 olivine + 0.23 orthopyroxene + 1.00 melt (Condamine et al., 2016). As shown in Fig. 10, most trace elements can be produced by 1-3% partial melting of the mica-bearing peridotite. Titanium of the AVB lavas is relatively enriched compared to the modeling results, which is reasonable because the AVB crust is significantly thicker than the crust beneath Monte Vulture, and thus more proportions of Ti-phlogopite are required to be stable in the AVB sources.

Figure captions

Fig. 1. Map of Tibetan Plateau showing post-collisional magmatic rocks and major terranes (modified from Yin and Harrison, 2000; Ding et al., 2003; Chung et al., 2005; Wu et al., 2020). The AVB and Pulu volcanic fields are located in the western Songpan-Ganzi terrane. From south to north, suture zones between the major terranes are Indus-Tsangpo Suture (ITS), Bangong-Nujiang Suture (BNS), Jinsha Suture (JS), Kunlun Suture (KS), South Qilin Suture (SQS). STDS = south Tibet detachment system; MBT = main boundary thrust.

Fig. 2. Thallium isotopes ($\varepsilon^{205}Tl$) of the leached and unleached samples. The grey dotted 1:1 line indicates no difference between leached and unleached values.

Fig. 3. Thallium chemical and isotopic compositions for the AVB lavas and literature values of arc, MORB, and OIB samples. Note that Tl concentration and Ce/Tl ratios are plotted on a logarithmic scale. Data are compiled from: arc (Nielsen et al., 2016, 2017a; Prytulak et al., 2013, 2017), MORB (Nielsen et al., 2006, 2014), and OIB (Brett et al., 2021).

Fig. 4. (a) Th/Rb versus Ce/Tl ratios for the AVB lavas. The grey field represents the average Ce/Tl and Th/Rb ratios for DMM (Ce/Tl = 1196±315, 1sd; Th/Rb = 0.147±0.051, 1sd; Jenner and O'Neill, 2012; Nielsen et al., 2014). (b) Ce/Tl versus $\varepsilon^{205}Tl$ of the AVB lavas.

Fig. 5. Pyrite grains in clinopyroxene phenocrysts and groundmass in the thin section of ASKL-3 by SEM (a-c). The major and minor concentrations of ASKL-3-1, ASKL-3-2, and ASKL-3-3 pyrite grains were measured by EPMA.

Fig. 6. Rb/Sr versus Tl concentrations of post-collisional lavas. Sample data of south Tibet and Anatalio are from Wang et al., (2020b) and Moghadam et al., (2018), respectively.

Fig. 7. (a) Tl versus MgO; (b) ε^{205}Tl versus MgO; (c) Tl versus Ce/Tl ratios; (d) Tl versus Rb of the AVB lavas.

Fig. 8. Thallium versus Sr (a) and Nd (b) isotopes for the AVB lavas. As isotopic data for the Tethys oceanic components are unavailable, only approximately trends for mixing between the DMM and oceanic components are shown. The Tl isotopic compositions of oceanic components are from Nielsen et al. (2017b).

Fig. 9. Cartoon model illustrating the formation of post-collisional lavas on Tibetan Plateau. (a) Before the Indian-Asian collision (55Ma), fluids and melts from Paleo- and Neo-Tethys oceanic subductions metasomatized the Tibetan lithospheric mantle, forming phlogopite-bearing peridotite veins. (b) Since ~55 Ma, due to the Indian-Asian collision and continuous underthrusting of the Indian Plate beneath the Tibetan Plateau, a series of complex plate geodynamic processes occurred on the Tibetan Plateau. These geodynamic processes, including convective thinning, delamination, slab roll-back and break-off, and shear heating, may induce partial melting of the metasomatized mantle and form a large amount of west-east extension of post-collisional magmatism belts in Tibet.

Fig. 10. Trace element batch melting modelling for mica-bearing peridotite, normalized to primitive mantle (McDonough and Sun, 1995). The most primitive samples with >6% MgO (ASKL-17 and ASKL-18) are plotted for comparison. Mineral modal abundances (melt modes in parentheses) for batch melting are: olivine 0.70(-0.06), orthopyroxene 0.2(-0.23), clinopyroxene 0.03(0.18), garnet 0.01 (0.52), phlogopite 0.06 (0.59). The D values are from the appendix table A4 of Williams et al. (2004).

Figure1

Click here to access/download;Figure;Fig1r.tif

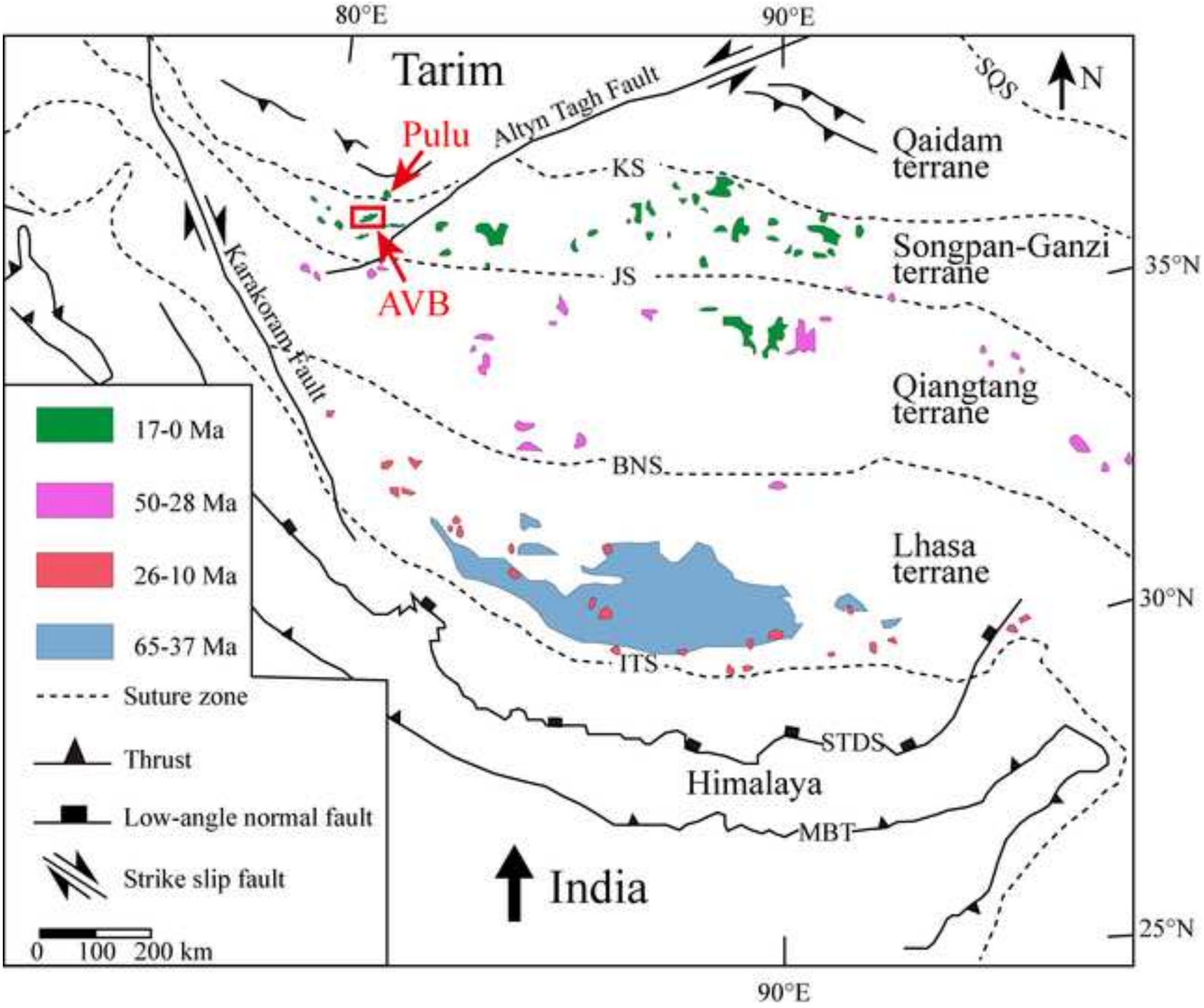

Figure2

Click here to access/download;Figure;fig2r.tif

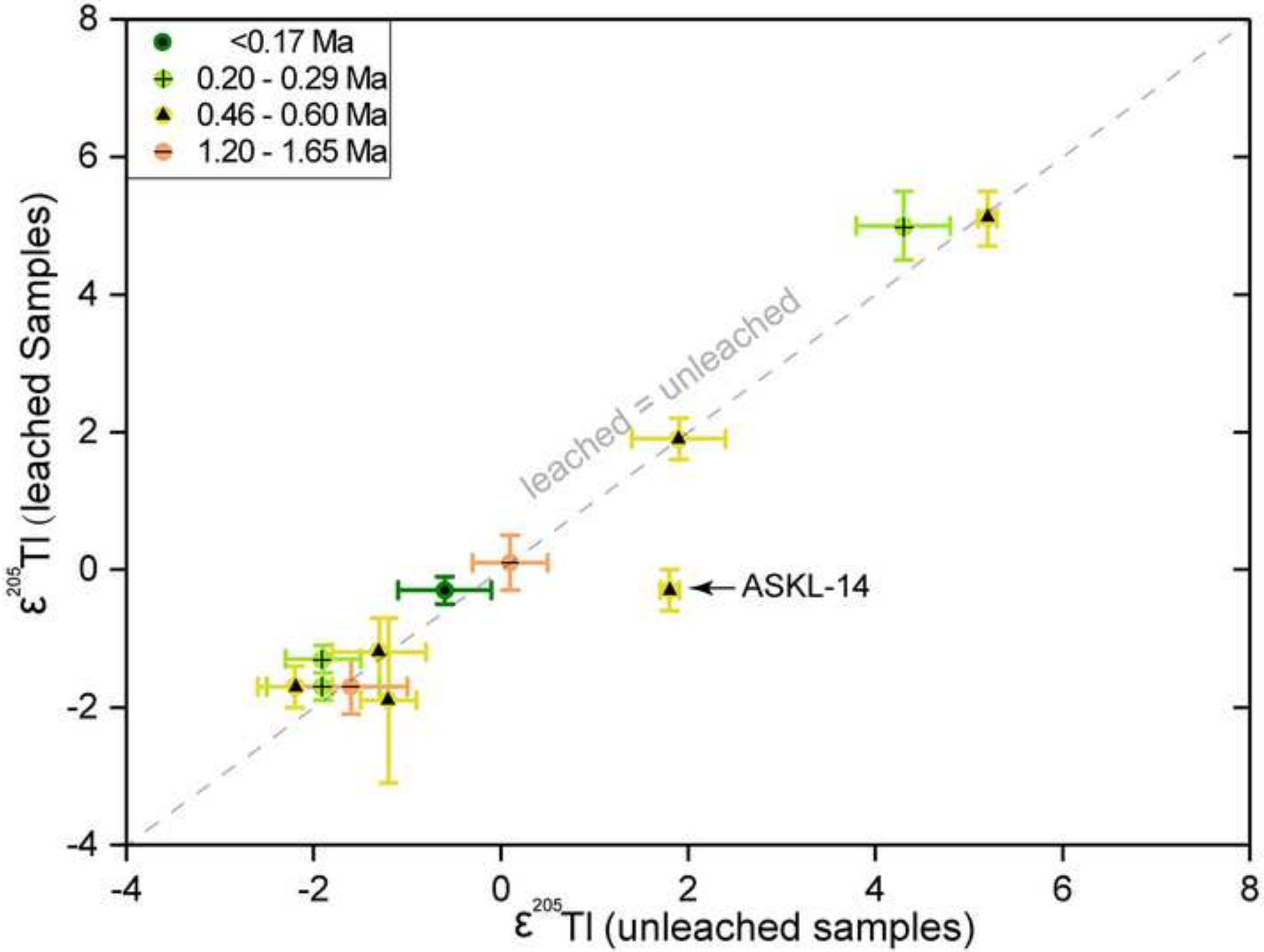

Figure3

Click here to access/download;Figure;Fig3r.tif

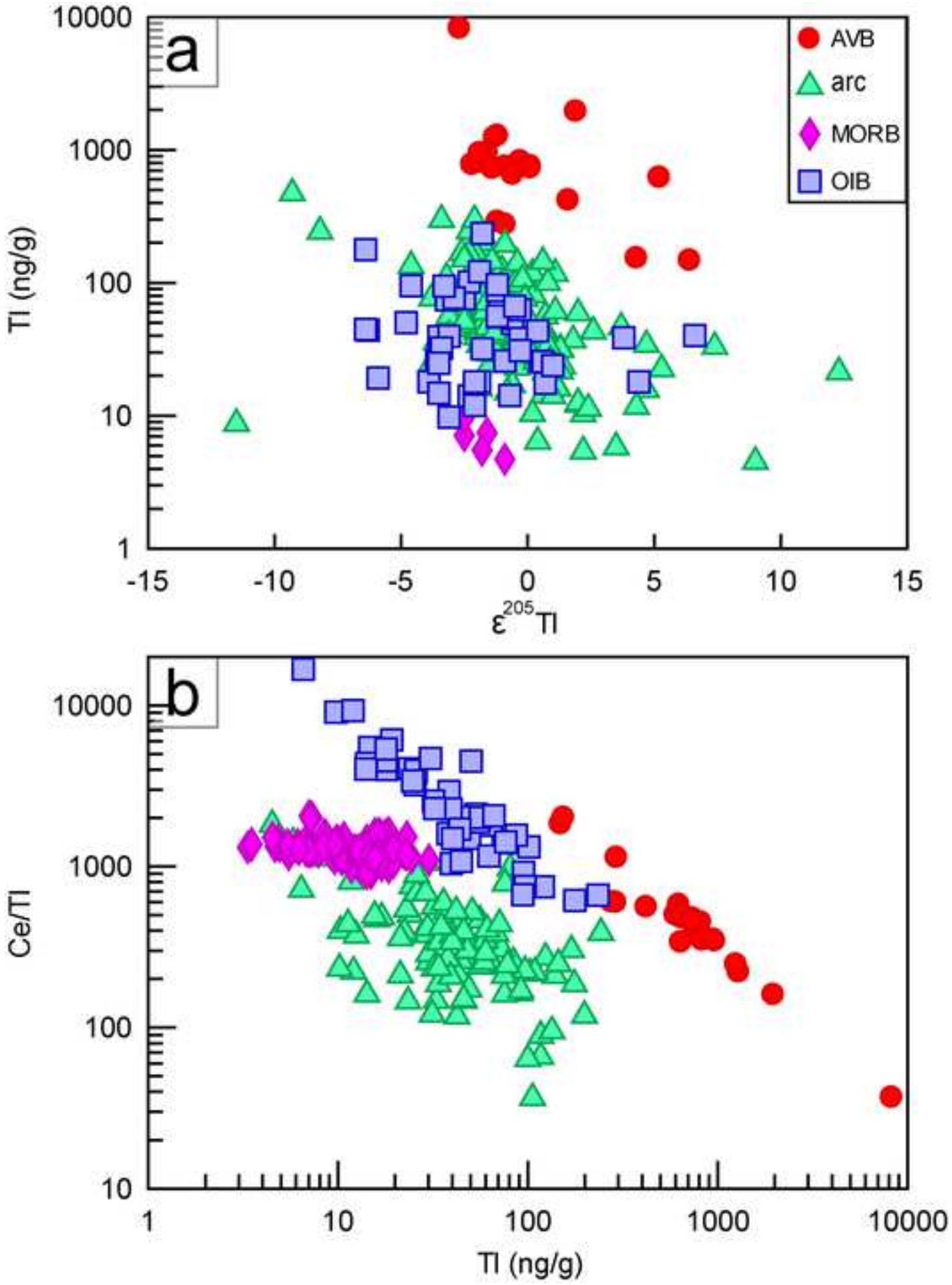

Figure4

Click here to access/download;Figure;fig4r.tif

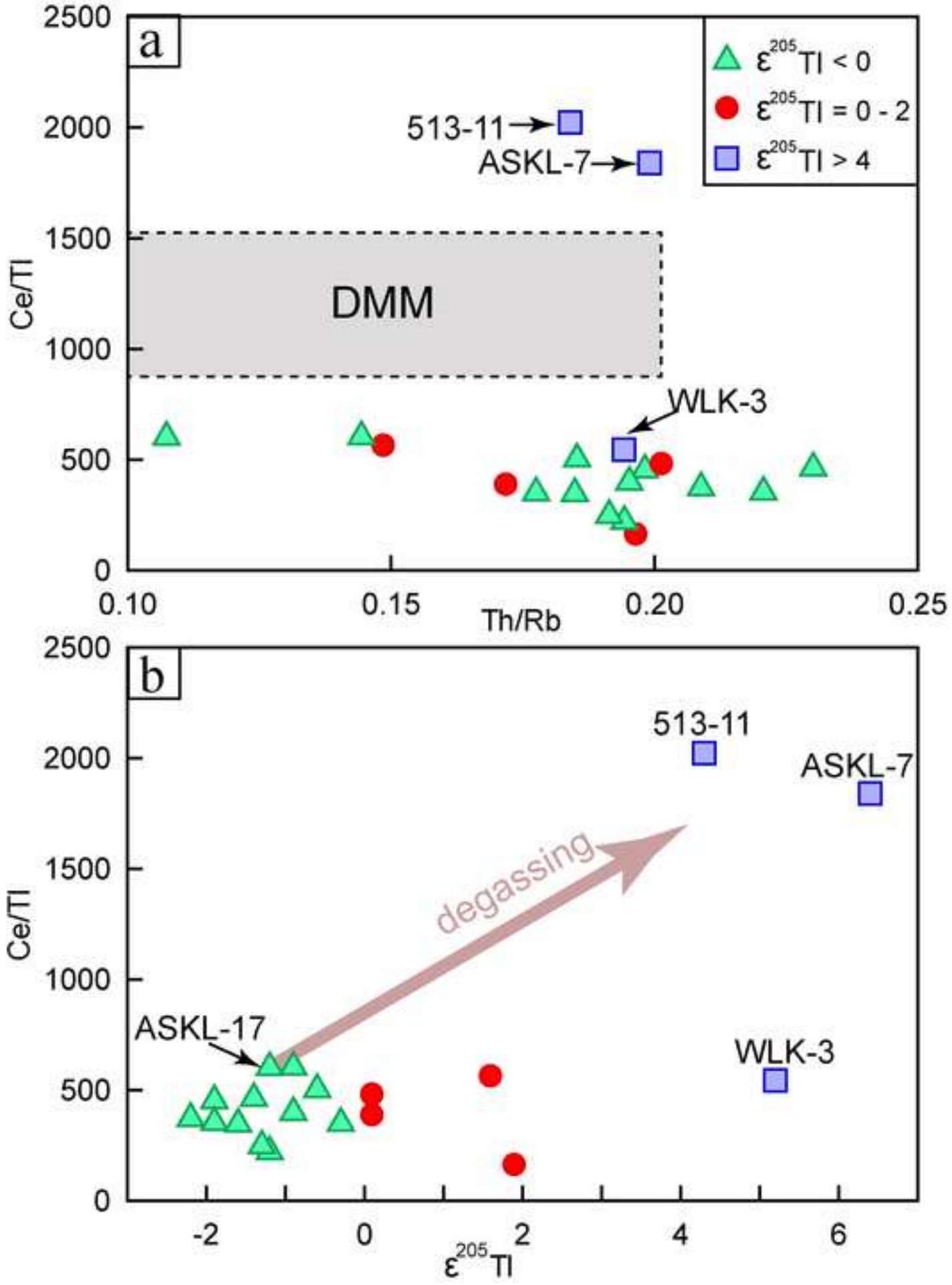

Figure5

Click here to access/download;Figure;Fig5r.tif

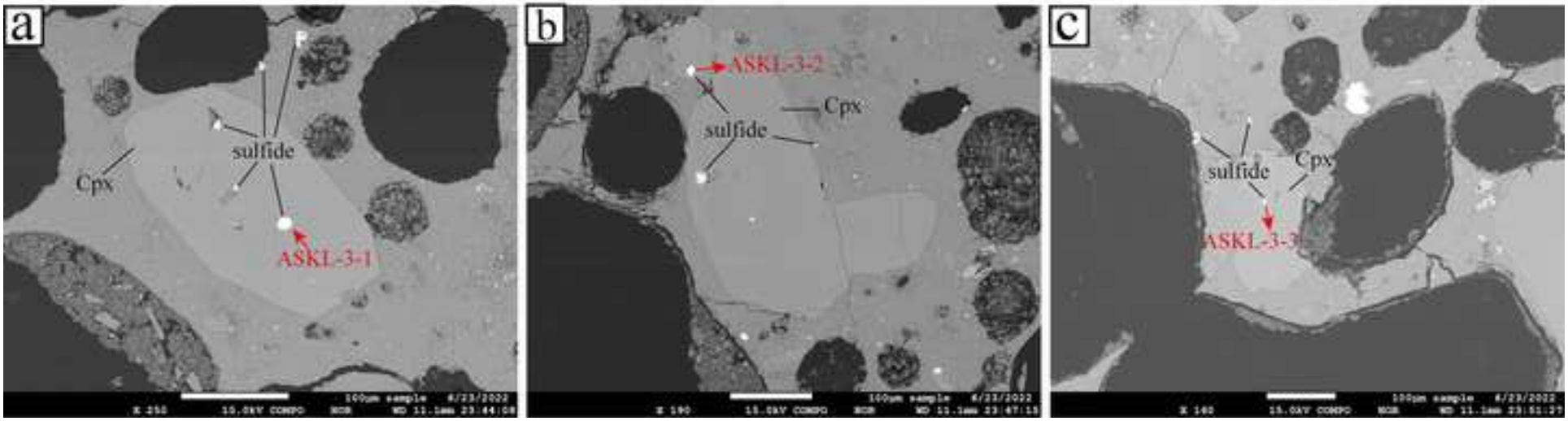

Figure6

Click here to access/download;Figure;Fig6r.tif

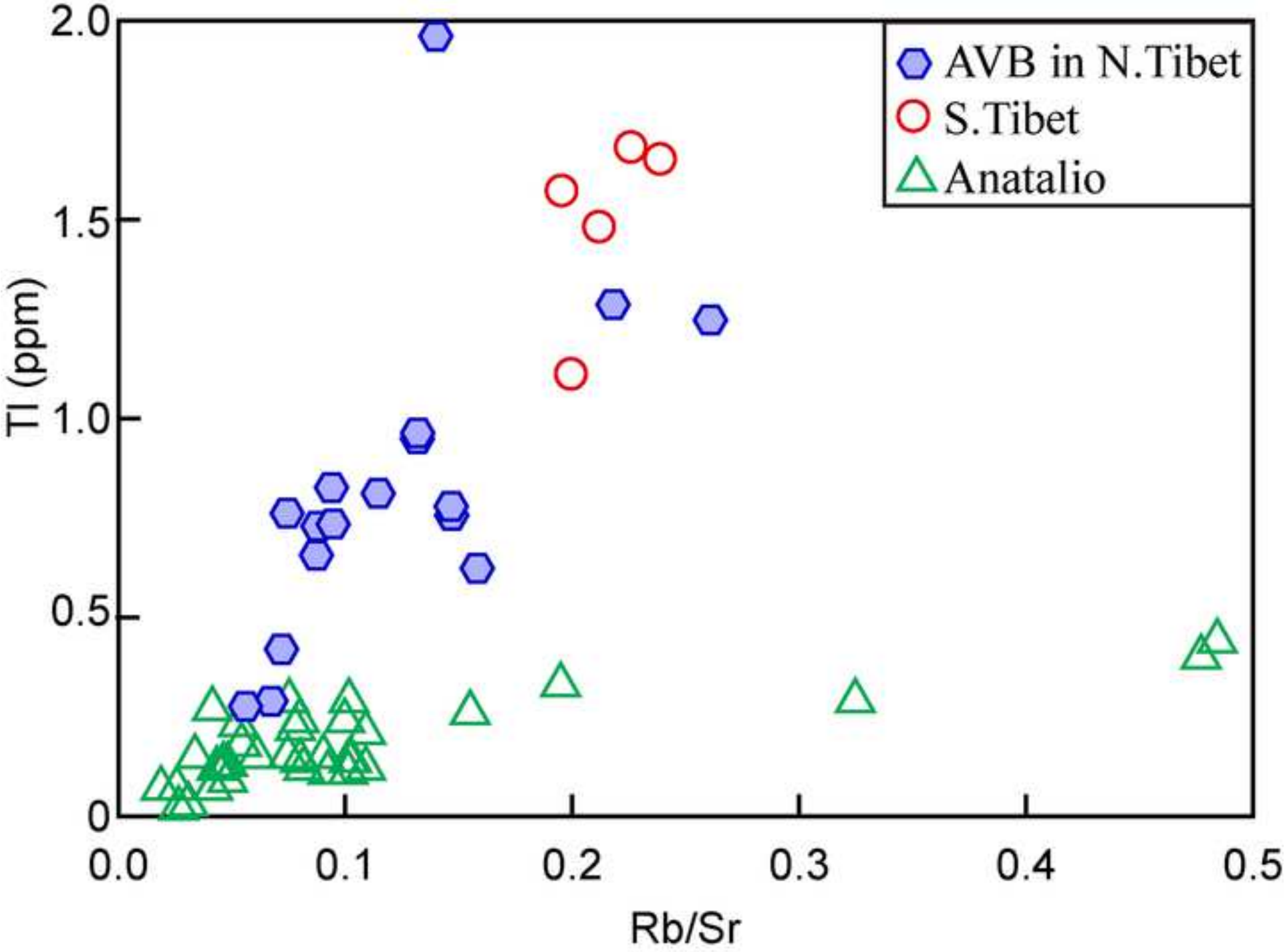

Figure7

Click here to access/download;Figure;Fig7r.tif

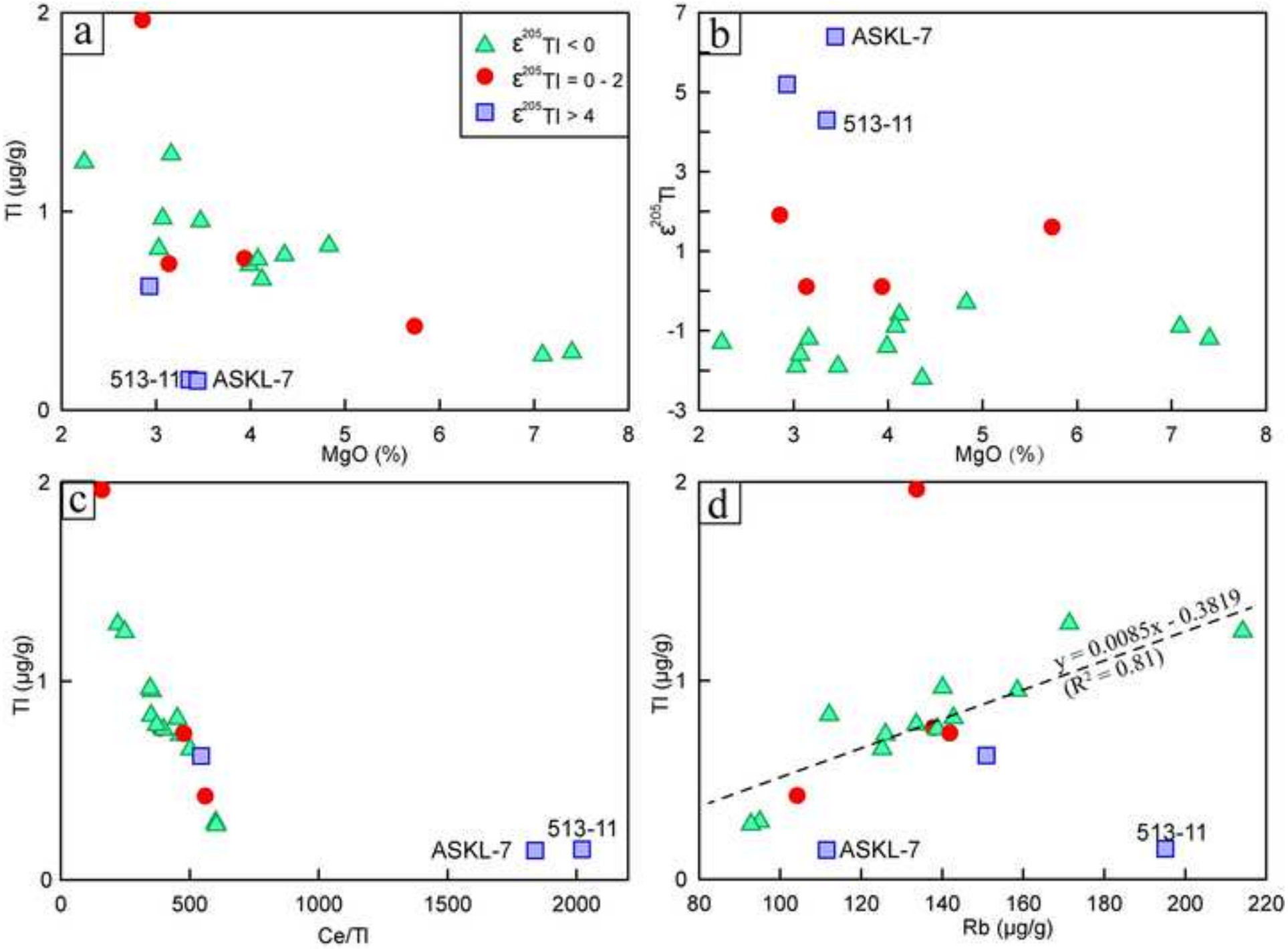

Figure8

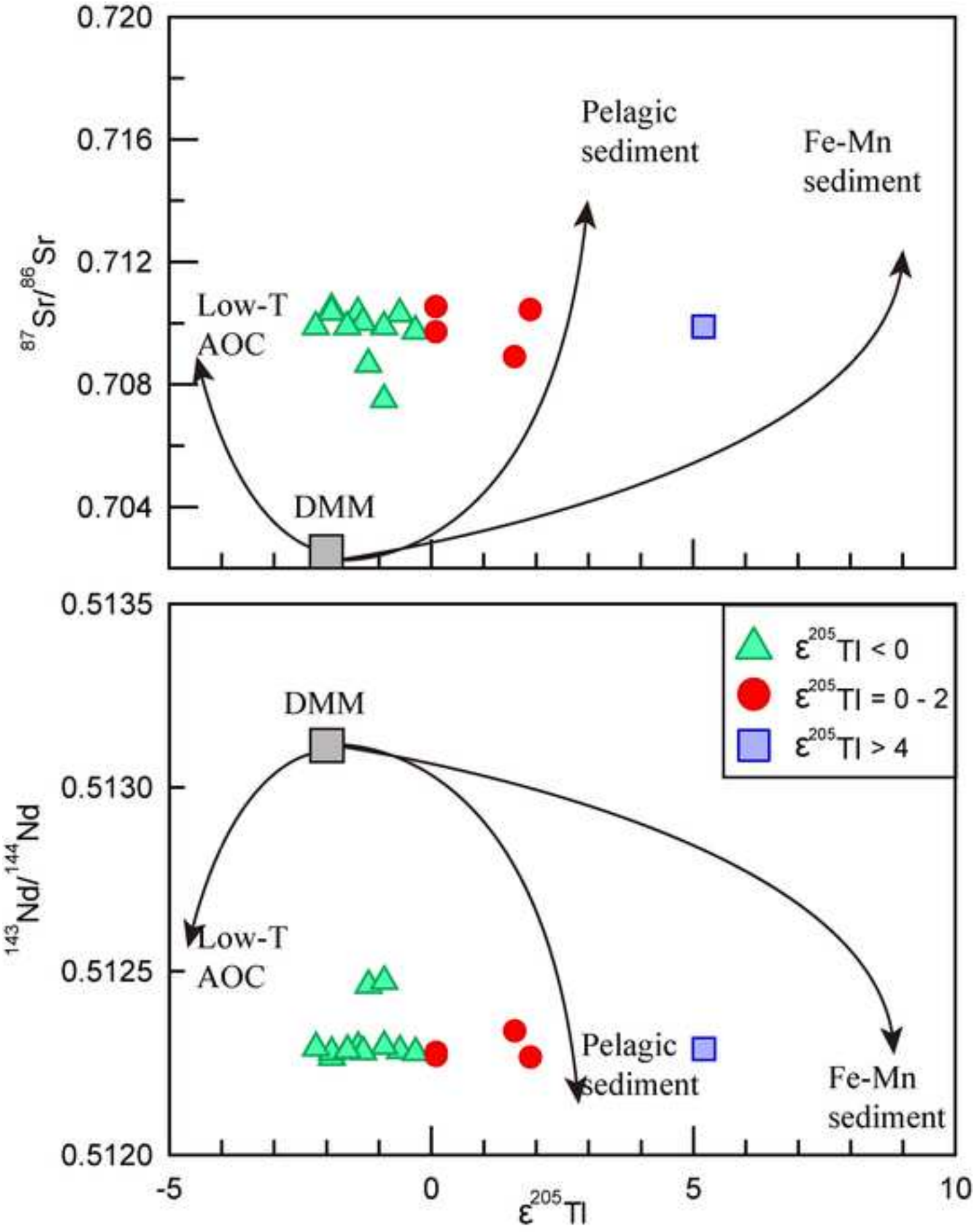

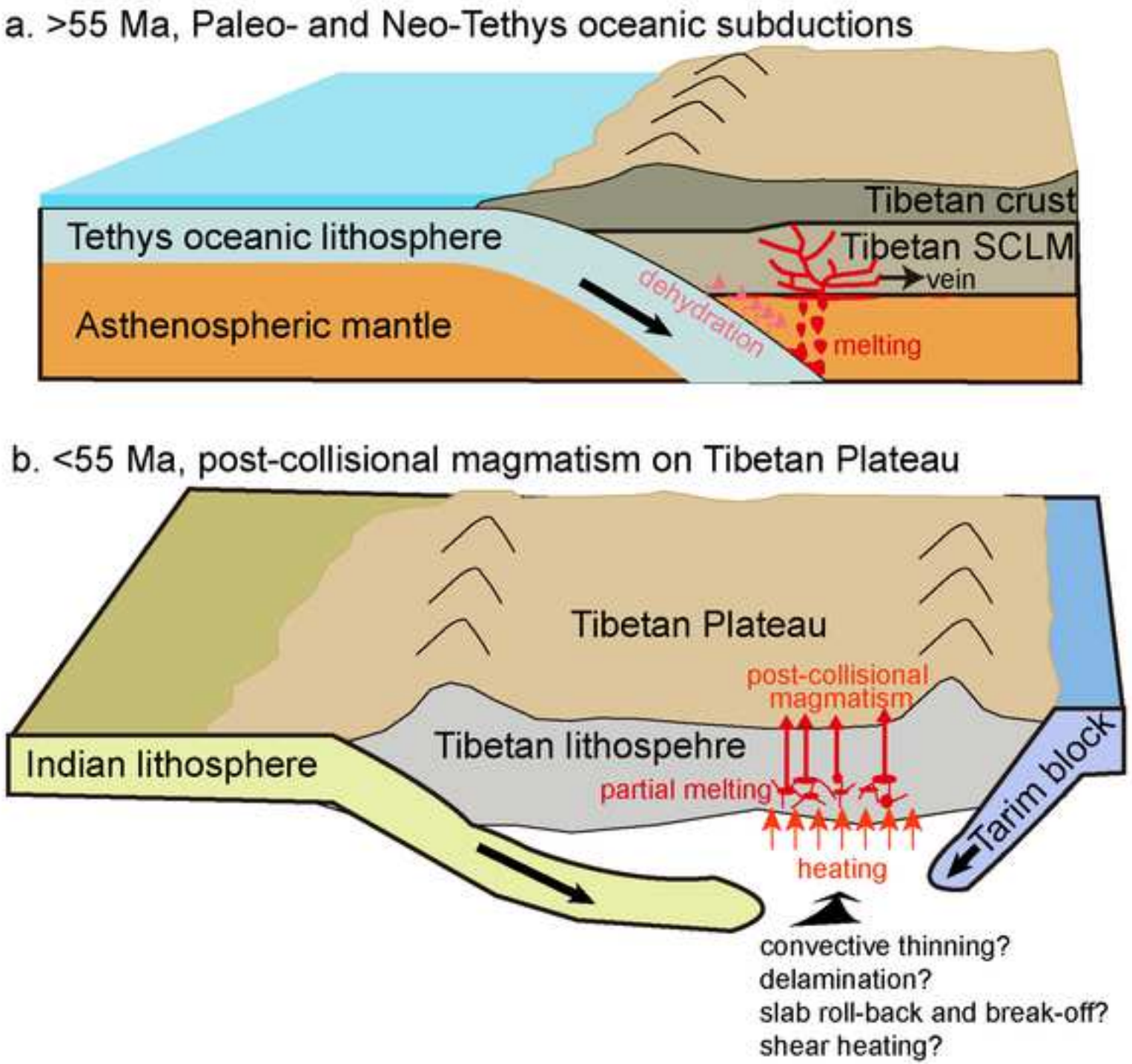

Figure10

Click here to access/download;Figure;Fig10r.tif

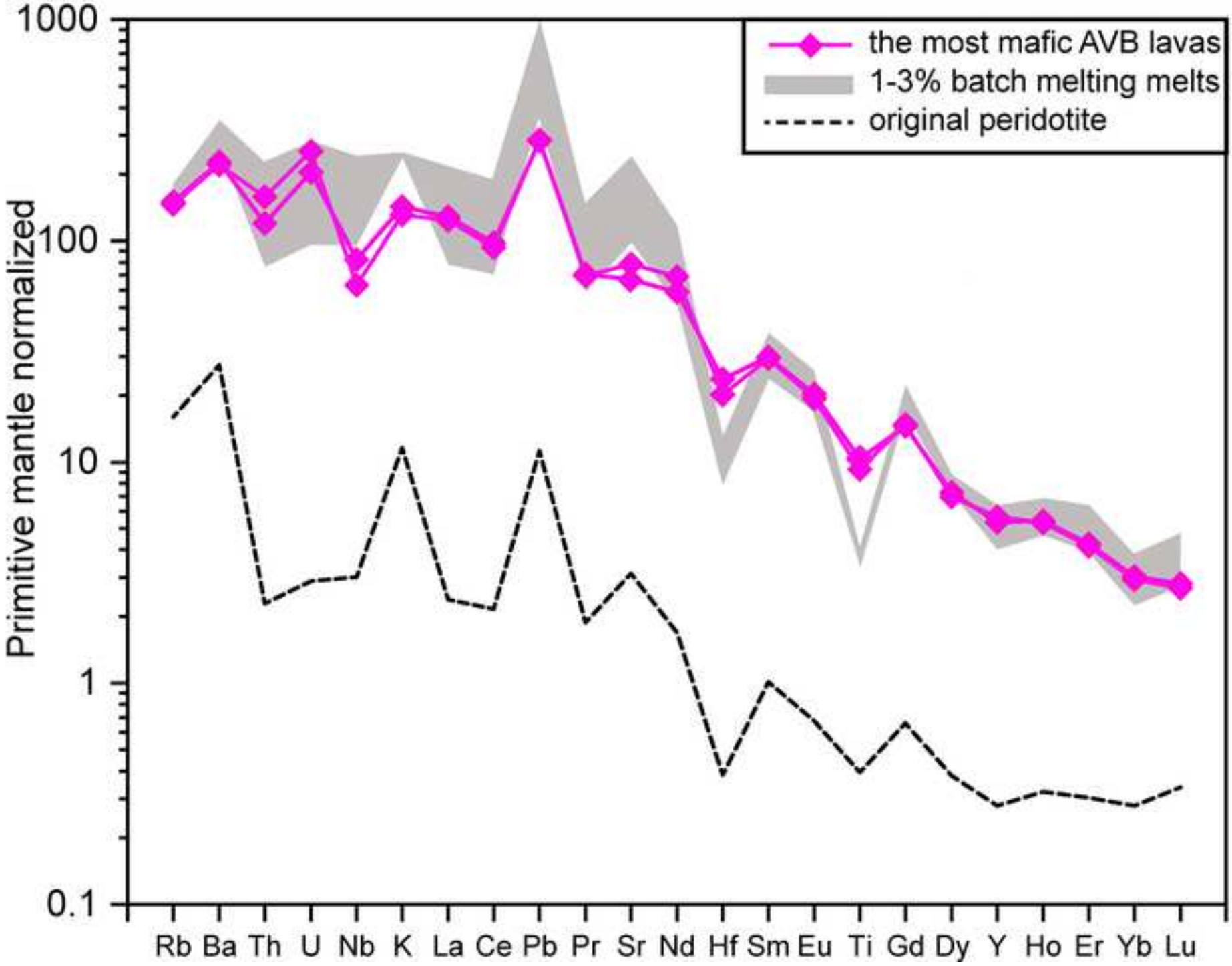

Table 1 Key elemental and petrographic features of AVB lavas

Episode (age)	Sample	Tl (ng/g)	K_2O (%)	Rb (μg/g)	LOI (%)	Vesicle (%)	Groundmass (%)	Phenocrysts (%)
1 and 2 (<0.17 Ma)	ASKL-3	8259	3.97	120	2.91	60	28	Pl(6)+Cpx(3)+Opx(2)+Ol(1)
1 and 2 (<0.17 Ma)	ASKL-4	656	4.07	125	1.48	55	32	Pl(1)+Cpx(4)+Opx(6)+Ol(1)+Bi(<1)+Fe-Ti(<1)
1 and 2 (<0.17 Ma)	518-5	729	4.19	126	0.96	35	51	Opx(9)+Cpx(4)+Pl(1)
3 (0.20-0.29 Ma)	ASKL-10	811	4.00	143	1.45	30	60	Pl(8)+Opx(1)+Fe-Ti(1)
3 (0.20-0.29 Ma)	513-11	154	4.30	195	1.27	45	40	Pl(10))+Cpx(2)+Opx(2)+Phl(1)
3 (0.20-0.29 Ma)	518-9	949	4.43	159	1.01	45	39	Pl(10)+Cpx(3)+Opx(2)+ Fe-Ti(1)
4 (0.46-0.60 Ma)	ASKL-7	148	3.98	116	2.86	20	65	Pl(12)+ Opx(2)+Cpx(<1)
4 (0.46-0.60 Ma)	ASKL-8	1960	4.20	134	1.03	25	42	Pl(25)+ Opx(4)+Cpx(2)+ Fe-Ti(2)
4 (0.46-0.60 Ma)	ASKL-12	1286	4.41	171	2.99	10	58	Pl(22)+ Opx(4)+Cpx(3)+Phl(1)+Fe-Ti(2)
4 (0.46-0.60 Ma)	ASKL-14	826	3.68	112	1.20	25	66	Pl(5)+Opx(4)
4 (0.46-0.60 Ma)	ASKL-15	761	3.94	138	1.54	30	52	Pl(7)+Cpx(6)+Opx(5)
4 (0.46-0.60 Ma)	ASKL-16	756	3.74	139	1.49	15	58	Pl(15)+Opx(8)+Cpx(2)+Phl(1)+Fe-Ti(1)
4 (0.46-0.60 Ma)	515-1	1247	4.47	214	1.95	15	68	Pl(12)+Opx(2)+Phl(2)+Cpx(1)
4 (0.46-0.60 Ma)	WLK-3	623	4.34	151	0.26	30	61	Pl(6)+Opx(2)+Ol(<1)+Fe-Ti(<1)
4 (0.46-0.60 Ma)	516-2	779	3.76	134	1.38	25	56	Cpx(11)+Opx(6)+Pl(2)
5 (1.02-1.65 Ma)	ASKL-5	734	4.03	142	1.50	50	34	Pl(11)+ Opx(2)+Fe-Ti(2)+Cpx(1)
5 (1.02-1.65 Ma)	516-11	420	3.72	104	3.21	40	48	Opx(6)+Cpx(3)+Pl(2)+Fe-Ti(1)
5 (1.02-1.65 Ma)	518-14	963	4.13	140	1.64	30	64	Pl(2)+Opx(2)+Cpx(1)+Fe-Ti(1)
6 (2.34-2.80 Ma)	ASKL-17	290	4.30	95	0.41	30	57	Cpx(9)+Opx(4)
6 (2.34-2.80 Ma)	ASKL-18	276	3.95	93	3.52	30	55	Cpx(12)+Opx(2)+Pl(1)

Chemical and petrographic data are from Wei et al. (2017). Pl = plagioclase; Cpx = clinopyroxene; Opx = orthopyroxene; Phl = phlogopite; Fe-Ti = Fe-Ti oxides; G = glass. Numbers in the brackets after the phenocrysts indicate the visually estimated volumetric percentages of the different phenocryst types in the thin section.

Table 2 Thallium concentration and isotopes of the AVB lavas.

Episode	Sample	$\varepsilon^{205}Tl$	n	Error (2σ)	Tl (ng/g)	Ce/Tl
1 and 2 (<0.17 Ma)	ASKL-3	-2.7	5	0.4	8259	37
1 and 2 (<0.17 Ma)	ASKL-4	-0.6	2	0.5	656	502
1 and 2 (<0.17 Ma)	518-5	-1.4	2	0.2	729	462
3 (0.20-0.29 Ma)	ASKL-10	-1.9	4	0.4	811	452
3 (0.20-0.29 Ma)	513-11	4.3	2	0.5	154	2022
3 (0.20-0.29 Ma)	518-9	-1.9	4	0.6	949	353
4 (0.46-0.60 Ma)	ASKL-7	6.4	3	0.8	148	1840
4 (0.46-0.60 Ma)	ASKL-8	1.9	2	0.5	1960	161
4 (0.46-0.60 Ma)	ASKL-12	-1.2	2	0.3	1286	221
4 (0.46-0.60 Ma)	ASKL-14	-0.3	2	0.3	826	350
4 (0.46-0.60 Ma)	ASKL-15	0.1	2	0.7	761	386
4 (0.46-0.60 Ma)	ASKL-16	-0.9	3	0.1	756	398
4 (0.46-0.60 Ma)	515-1	-1.3	3	0.5	1247	248
4 (0.46-0.60 Ma)	WLK-3	5.2	2	0.1	623	544
4 (0.46-0.60 Ma)	516-2	-2.2	3	0.4	779	372
5 (1.02-1.65 Ma)	ASKL-5	0.1	4	0.4	734	479
5 (1.02-1.65 Ma)	516-11	1.6	4	0.8	420	562
5 (1.02-1.65 Ma)	518-14	-1.6	6	0.6	963	346
6 (2.34-2.80 Ma)	ASKL-17	-1.2	2	0.7	290	601
6 (2.34-2.80 Ma)	ASKL-18	-0.9	2	0.5	276	603

Table 3 EPMA measurements (wt.%) of pyrites in the thin section of ASKL-3

ID	As	Se	Fe	Ni	Cu	Zn	Pb	S	Tl
ASKL-3-1	b.d.	0.016	56.9	3.1	0.039	b.d.	b.d.	39.6	b.d.
ASKL-3-2	b.d.	0.021	57.5	2.6	b.d.	b.d.	0.072	39.3	b.d.
ASKL-3-3	b.d.	b.d.	57.4	2.0	0.004	b.d.	0.012	39.9	b.d.

b.d.: below the detection limit